PIPELINE ROBOTICS
AERIAL SERVICES
RESEARCH AND DEVELOPMENT
ENERGY SERVICES

Contract # DTPH5616T00004

EMAT Guided Wave Technology for Inline Inspections of Unpiggable Natural Gas Pipelines

PUBLIC REPORT

Report Date: September 26, 2018

Prepared For:
U.S. Department of Transportation
Pipeline and Hazardous Materials Safety Administration
Office of Pipeline Safety
Joshua Arnold
202-366-6085
joshua.arnold@dot.gov

ULC Robotics Team:

Name	Title	Email address
Dr. Baiyang Ren	Principal Investigator, Sensor Scientist	bren@ulcrobotics.com
Dr. Junjun Xin	Senior Sensor Scientist	jxin@ulcrobotics.com
Aalap Shah	Project Manager	ashah@ulcrobotics.com

ULC ROBOTICS
88 Arkay Drive
Hauppauge, NY 11788
www.ulcrobotics.com

TABLE OF CONTENTS

LIST OF FIGURES

LIST OF TABLES

1 EXECUTIVE SUMMARY

Under this project, ULC Robotics developed compact, lightweight, prototype Electro Magnetic Acoustic Transducers (EMATs) and studied guided waves for defect detection, classification, and characterization in cast iron and steel pipes. Through lab testing, design, and Finite Element Analysis (FEA), guided wave propagation and defect interactions were evaluated, and the results were employed to optimize the prototype EMATs through successive design and testing iterations. The goal of developing EMATs for robotic inspection of unpiggable pipe was successfully achieved and demonstrated not only through prototype fabrication and testing but also through conceptual design modifications to ULC's CIRRIS XI^{TM} robot that incorporated EMATs onto the robot.

The guided wave EMAT sensor will be capable of offering superior anomaly detection performance and coverage when integrated with Inline Inspection (ILI) tools or with ULC's proven CIRRIS XI^{TM} inspection robot. These EMATs can be used in both small and large diameter pipelines. Utilizing the newly developed sensor, the CIRRIS XI^{TM} robot will be capable of providing 100% inspection coverage and flaw detection in unpiggable cast-iron mains. Moreover, by performing 100% inspection from within the pipe, faster inspection times can be achieved; ultimately lowering the cost of inspection while increasing the confidence of detecting threats.

The project began with testing and evaluating guided waves on cast iron and steel plates during which the baseline set of assumptions and approximate sensor design parameters were developed. During subsequent pipe testing, techniques were developed for determining the baseline signal and identifying defect signatures. ULC developed post-processing methods for the raw EMAT sensor signals that enabled detecting and classifying defects which in practice can aid the ILI tool or robot operator in identifying these threats immediately after the inspection run is performed. Influencing factors were determined that affect sensor performance. These influencing factors dictate the sensor arrangement on the tool or robot and the operational methods for the robot or tool. Two special cases: buried pipes in soil and in the presence of large amounts of corrosion debris were also tested and evaluated to study the effects on guided wave propagation and defect sensitivity.

The next steps recommended for the further study of guided wave EMAT include evaluating the effects of pipe coatings on defect sensitivity and studying other defects such as pitting corrosion, general metal loss, and de-laminations. The recommended next steps for commercialization of guided wave EMAT include developing miniature pulsing and receiving electronics for integration into robotic systems and tools catered to unpiggable pipe and small diameter pipe. Testing on more real-world samples such as those offered by PRCI would help improve the post-processing methods and increase the confidence in accurately detecting and classifying defects. Additional improvements can also be made to the EMAT housing to maintain constant liftoff and minimize pipe cleaning requirements.

The guided wave EMATs and the defect detection, classification, and assessment algorithms developed during the course of this project have great potential in enhancing the operator's ability to inspect 100% of the pipe and identify threats immediately so that appropriate remedial actions can be taken by the pipeline operator.

2 INTRODUCTION

The Pipeline and Hazardous Materials Safety Administration (PHMSA) awarded ULC Robotics the project titled "Electro Magnetic Acoustic Transducer (EMAT) guided wave sensor for inline inspection of unpiggable gas pipelines." This public report details the work performed under this project.

Currently available inline inspection technologies today cannot perform a complete inspection of unpiggable pipeline since they are unable to continuously scan all points in the pipeline in a reasonable timeframe. This timeframe is important to operators because the number of hours or days over which an inspection is performed has implications not only on the cost the operator must bear but also on the safety of individuals involved in the inspection operation. By speeding up the inspection process, guided wave EMAT has great potential in reducing the cost and improving the safety of inspections.

Under this project, ULC evaluated Guided Wave EMAT for both unpiggable cast iron and steel, distribution, and transmission mains and performed conceptual design for integrating the EMATs with the CIRRIS XI^{TM} robot. The CIRRIS XI^{TM} robot was developed by ULC on a separate project for deploying wall thickness EMAT sensors into 24” to 30” cast iron distribution mains. During the current project, ULC performed conceptual design for modifying the robot to incorporate the prototype guided wave EMATs.

This report walks through the design process employed for developing the guided wave EMAT and the testing performed and results from plate testing and pipe testing. Defect detection and baseline signal determination are described along with influencing factors. Results of soil testing and testing in the presence of corrosion debris have also been provided. A brief description is provided about the conceptual design description for the CIRRIS XI^{TM} robot that deploys guided wave EMATs.

A set of recommendations for future work are documented at the end of the report.

3 DISPERSION ANALYSIS AND MODE SELECTION

3.1 Dispersion analysis

Dispersion analysis is the identification of the relationship among frequency, wavenumber, phase velocity and group velocity. Such a relationship is represented by dispersion curves. In this study, the dispersion curves are always represented as frequency-phase/group velocity plots. Dispersion curves define the wave propagation characteristics of the wave propagation and provide useful information on mode selection and is thus usually the most fundamental study for any guided wave research.

In this work, dispersion curves were calculated using a semi-analytical finite element (SAFE) code written in MATLAB language. Phase velocity and group velocity dispersion curves were derived through the dispersion analysis and used for mode selection.

Plates and pipes (listed in Table 1) were studied and tested in this project. Dispersion curves are presented in this section. Comments on the characteristics of the dispersion curves are also provided here.

Table 1. Specimen geometry, material and dimensions tested in the project.

Structure	Material	Thickness (inch)	Diameter (inch)
Plate	Steel	0.25	N/A
Plate	Steel	0.5	N/A
Plate	Cast Iron	0.25	N/A
Pipe	Steel	0.5	12.75
Pipe	Steel (Seamless)	0.5	24
Pipe	Steel (ERW)	0.5	24
Pipe	Cast Iron	0.5	25.8

Table 2. Material properties of carbon steel and cast iron for dispersion analysis

Material	Mass density (kg/m^3)	Young's modulus (GPa)	Poisson's ratio
Carbon Steel	7870	205	0.29
Cast Iron	7200	120	0.29

3.1.1 0.25-inch steel plate

For a flat plate made of isotropic material, i.e., steel, there are mainly two categories of guided waves, namely Lamb and Shear Horizontal (SH) waves. Lamb wave vibrations are completely within the sagittal plane, and the SH wave vibrations are perpendicular to the sagittal plane. The phase velocity dispersion curves for the Lamb waves (Figure 1) and shear-horizontal (SH) waves (Figure 2) of a 0.25-inch thick steel plate are calculated and plotted. The group velocity dispersion curves for the Lamb waves (Figure 3) and shear-horizontal (SH) waves (Figure 4) of a 0.25-inch thick steel plate are calculated and plotted.

For most Lamb and SH wave modes, since the velocity varies with frequency, the wave is described as "dispersive." For any real-world wave excitation with a finite length of pulse, the wave packet will contain multiple frequency components, and the strongest component is the center frequency which corresponds to the excitation pulse frequency. It is thus expected that the excited wave packet will spread as it is propagating because different frequency components travel with different velocities. It is noted that the SH0 mode is non-dispersive since its velocity is independent of frequency. Also, there are low dispersive modes whose velocity changes slightly with changes in frequency. These are preferred features of guided wave modes since the wave packet will not distort too much over a long distance of propagation.

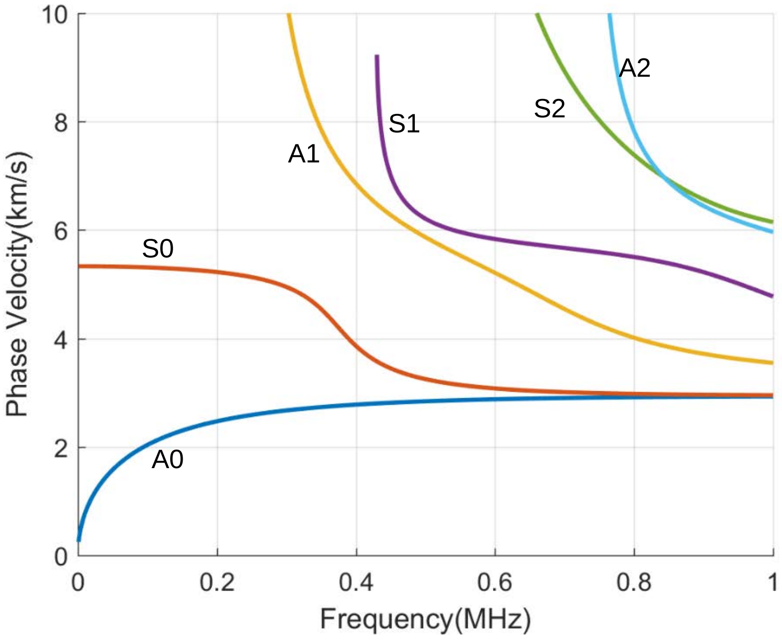

Figure 1: Lamb Wave Phase Velocity Dispersion Curves for the 0.25 inch Steel Plate

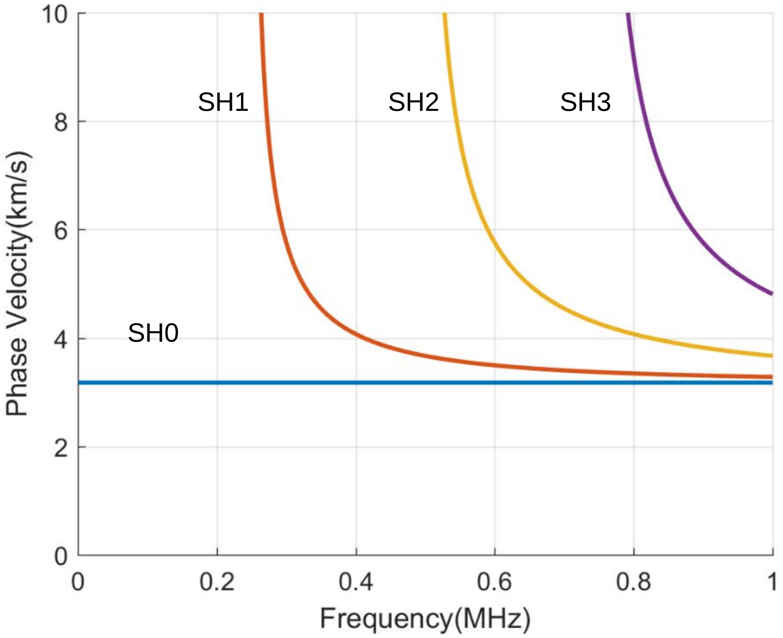

Figure 2: Shear Horizontal Wave Phase Velocity Dispersion Curves for the 0.25 inch Steel Plate

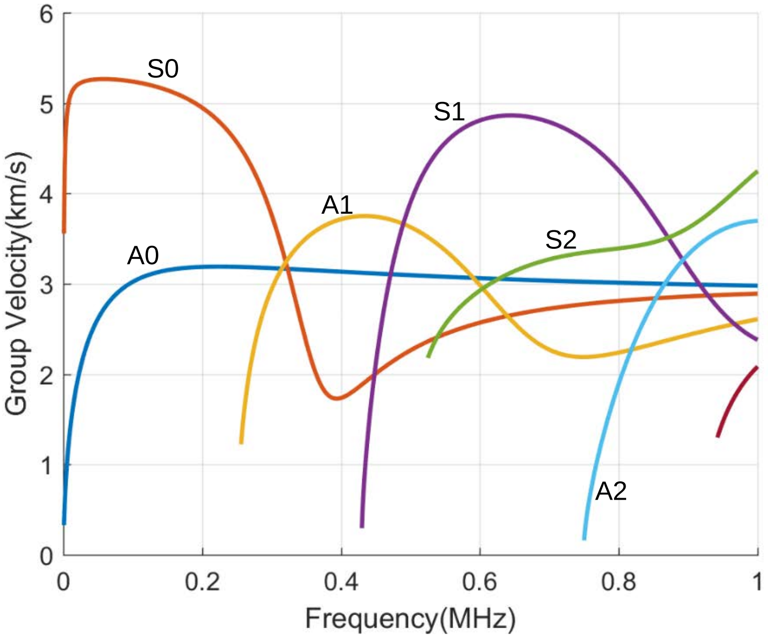

Figure 3: Lamb Wave Group Velocity Dispersion Curves for the 0.25 inch Steel Plate

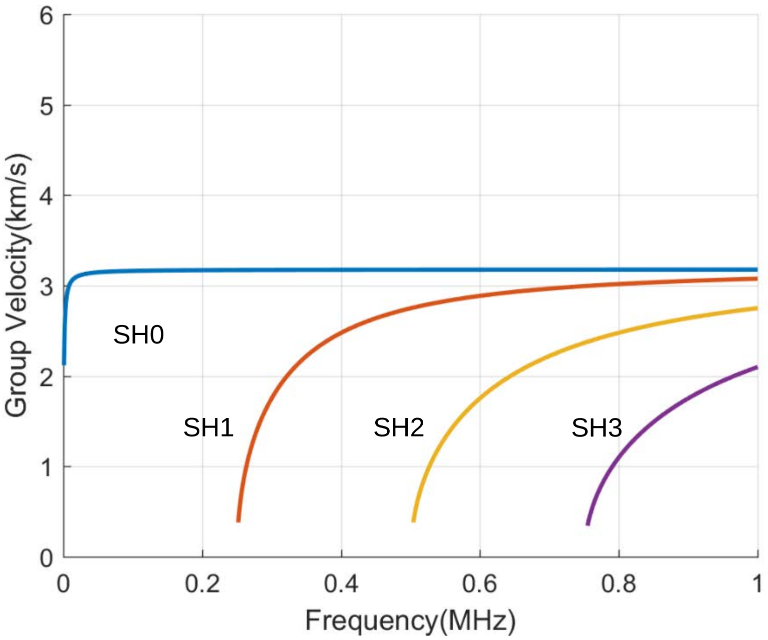

Figure 4: Shear Horizontal Wave Group Velocity Dispersion Curves for the 0.25 inch Steel Plate

3.1.2 0.5-inch steel plate

From Figure 5 to Figure 8, the phase and group velocity dispersion curves are plotted for the 0.5-inch steel plate. By comparing Figure 1 and Figure 5, it is noticed that for the same frequency range from 0 to 1 MHz, the thick steel plate has more wave modes than the thin plate. Also, to excite a particular mode with a certain phase velocity, it requires lower frequency for thick plates.

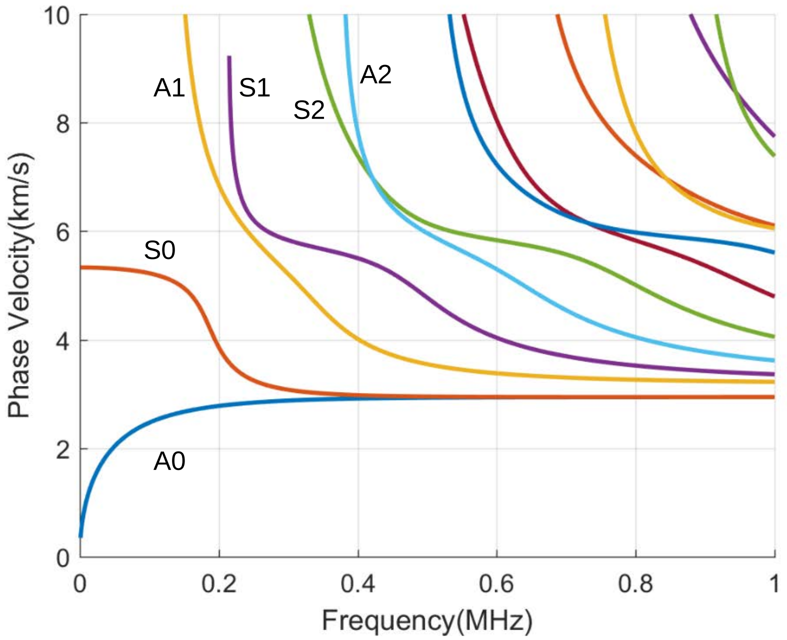

Figure 5: Lamb Wave Phase Velocity Dispersion Curves for the 0.5 inch Steel Plate

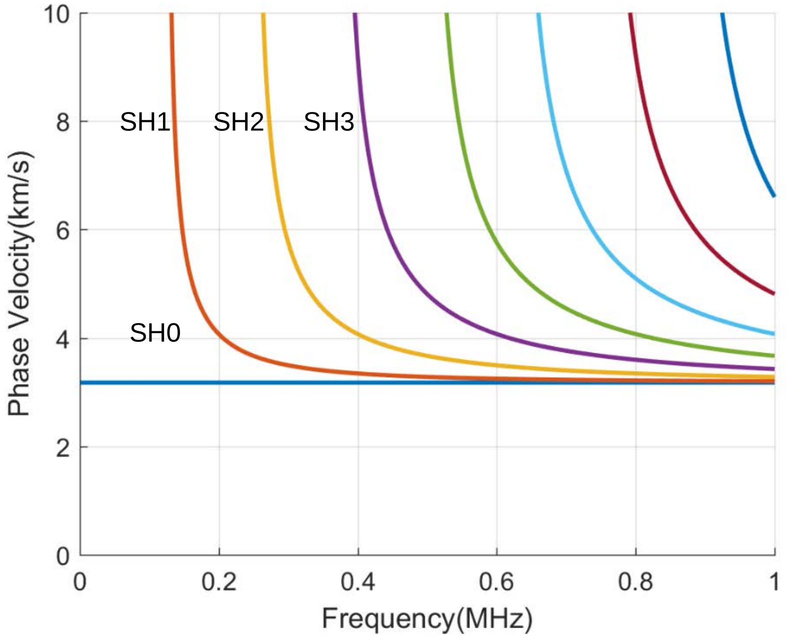

Figure 6: Shear Horizontal Wave Phase Velocity Dispersion Curves for the 0.5 inch Steel Plate

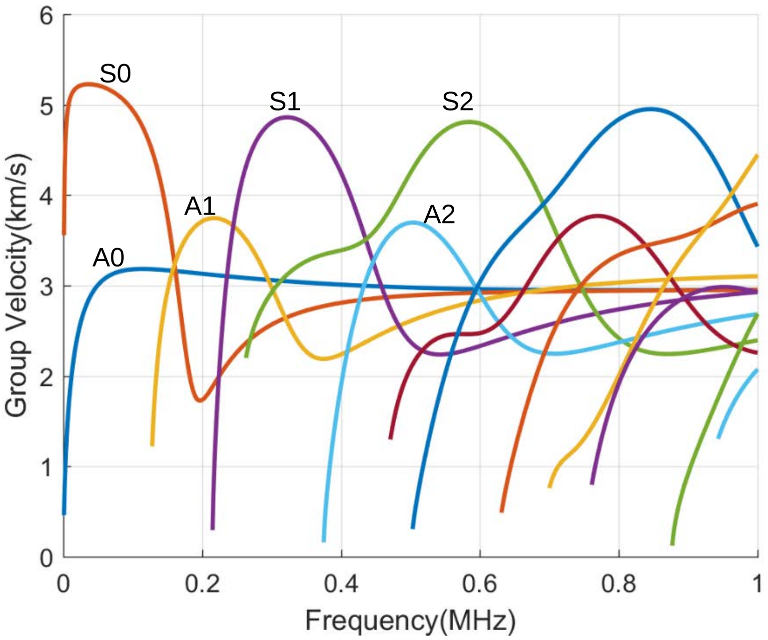

Figure 7: Lamb Wave Group Velocity Dispersion Curves for the 0.5 inch Steel Plate

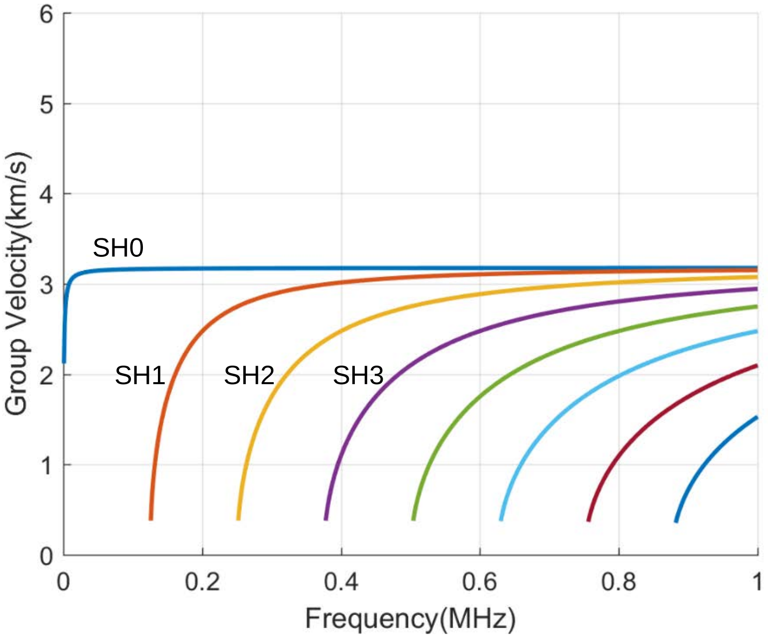

Figure 8: Shear Horizontal Wave Group Velocity Dispersion Curves for the 0.5 inch Steel Plate

3.1.3 0.25 inch cast iron plate

From Figure 9 to Figure 12, the phase and group velocity dispersion curves are plotted for the 0.25 inch cast iron plate. It is observed that the cast iron plate has lower phase and group velocity compared with the 0.25-inch steel plate. This is because the cast iron has a lower elastic modulus - see Table 2. Also, the cast iron plate has more guided wave modes than the 0.25-inch steel plate in the same frequency range, i.e., 0 to 1 MHz.

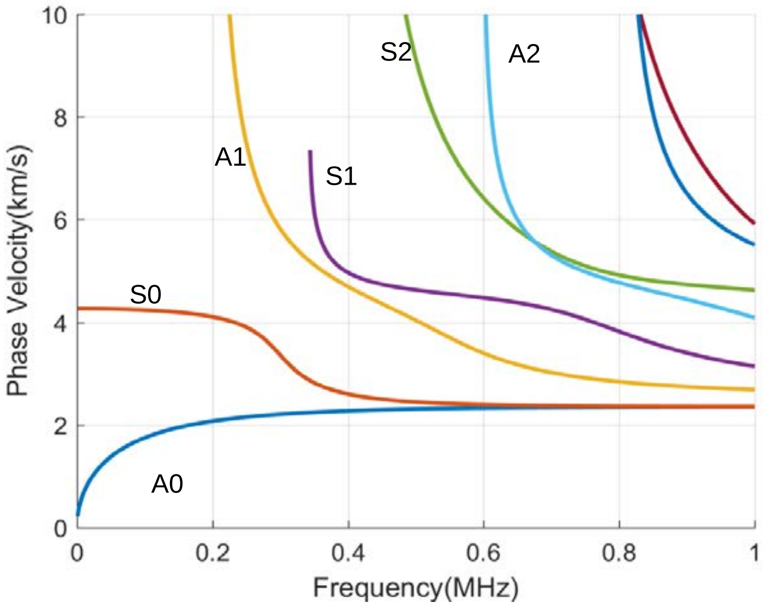

Figure 9: Lamb Wave Phase Velocity Dispersion Curves for the 0.25 inch Cast Iron Plate

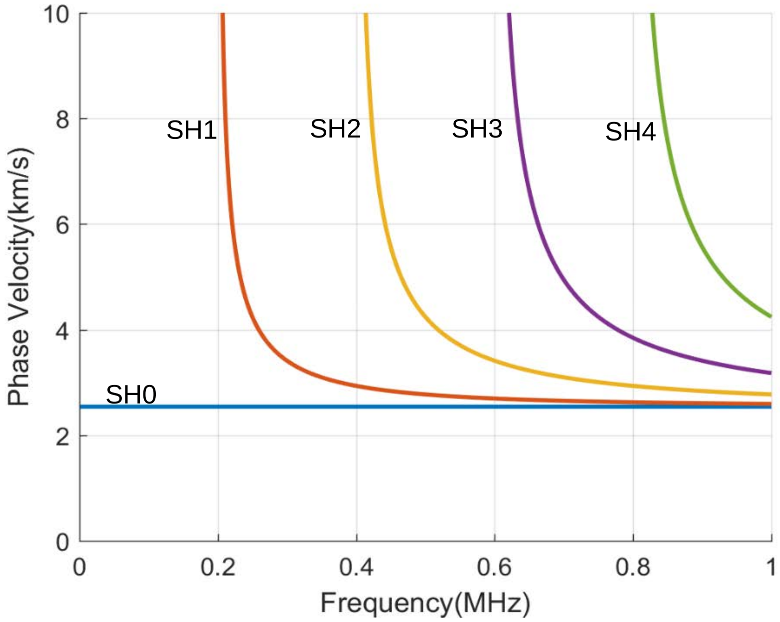

Figure 10: Shear Horizontal Wave Phase Velocity Dispersion Curves for the 0.25 inch Cast Iron Plate

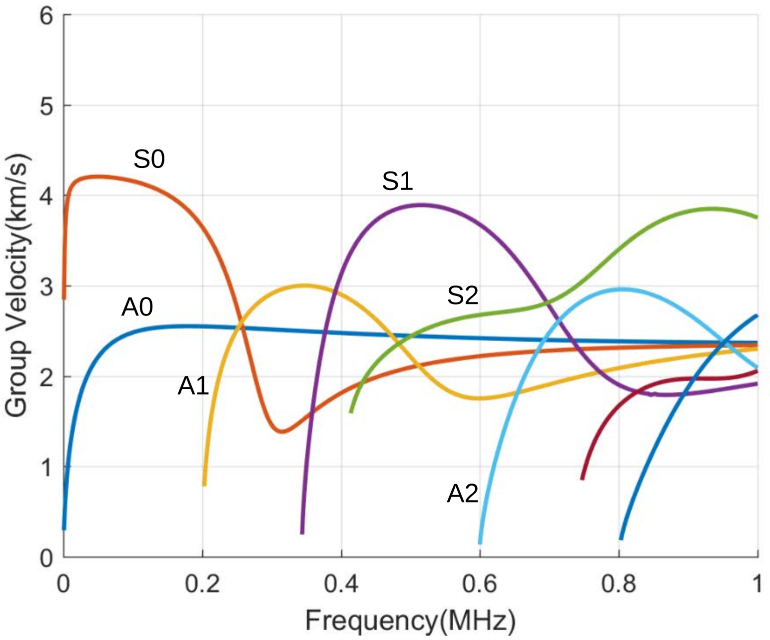

Figure 11: Lamb Wave Group Velocity Dispersion Curves for the 0.25 inch Cast Iron Plate

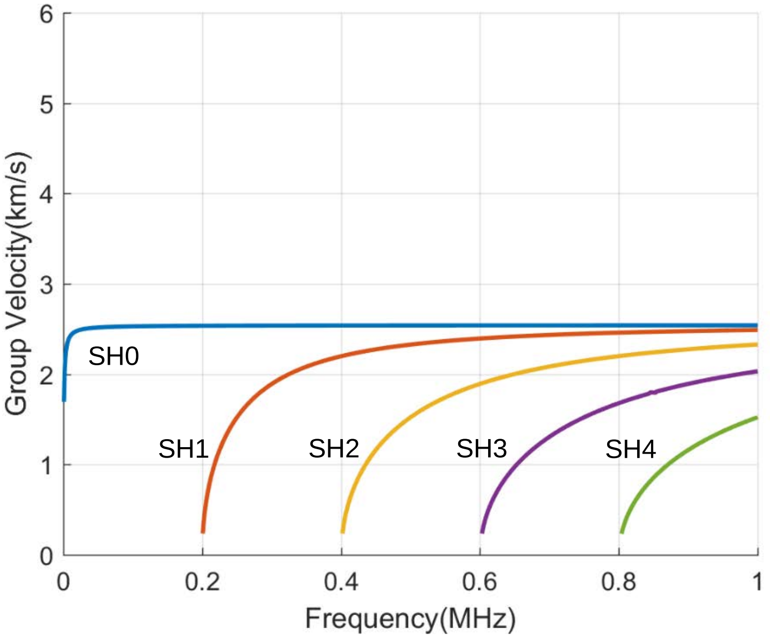

Figure 12: Shear Horizontal Wave Group Velocity Dispersion Curves for the 0.25 inch Cast Iron Plate

3.1.4 12-inch steel pipe with 0.5-inch wall

Phase velocity dispersion curves for the 12-inch steel pipe with 0.5-inch wall are plotted in Figure 13 and Figure 14. The phase velocity curves are very similar between the 0.5-inch plate and 0.5-inch pipe. Only a slight difference exists between these two structures. The group velocity curves are not shown here to limit the size of this report.

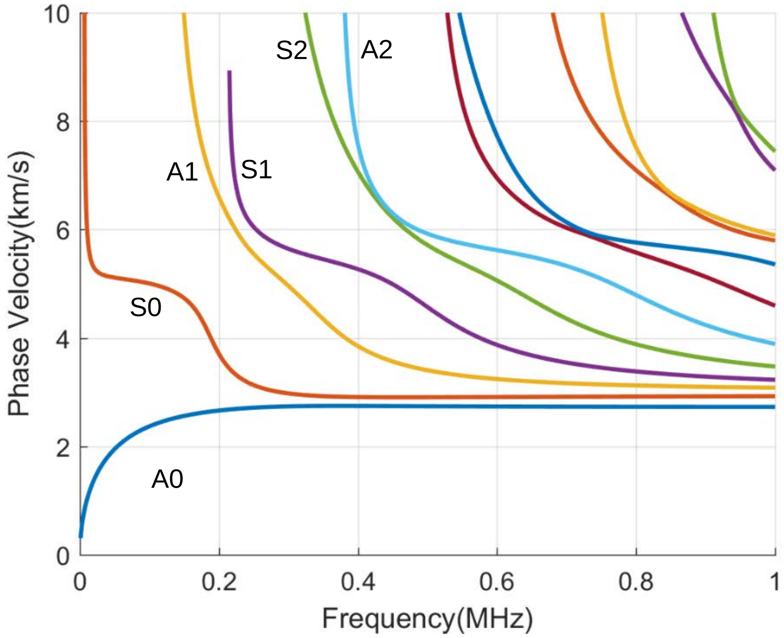

Figure 13: Lamb Wave Phase Velocity Dispersion Curves for the 12-inch steel pipe with 0.5-inch wall

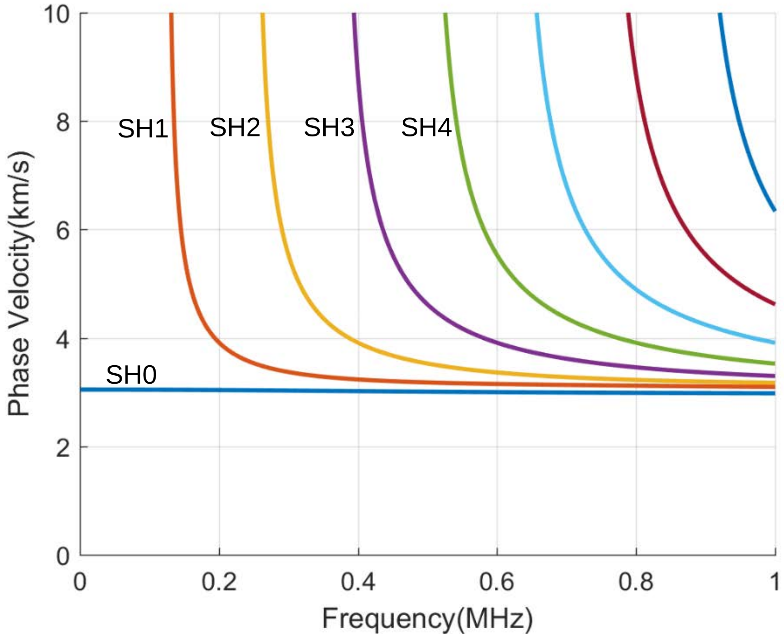

Figure 14: Shear Horizontal Wave Phase Velocity Dispersion Curves for the 12-inch steel pipe with 0.5-inch wall

3.1.5 24-inch steel pipe with 0.5-inch wall

The phase velocity dispersion curves for both 24-inch seamless and ERW pipes, are the same and are plotted in Figure 15 and Figure 16. Again, the dispersion curves are very similar to that of the plate and 12-inch pipe.

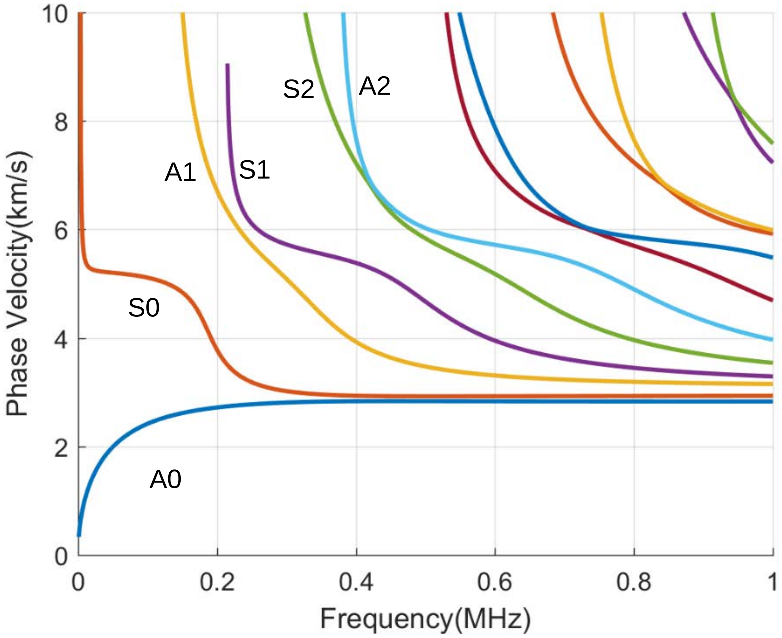

Figure 15: Lamb Wave Phase Velocity Dispersion Curves for the 24-inch steel pipe with 0.5-inch wall

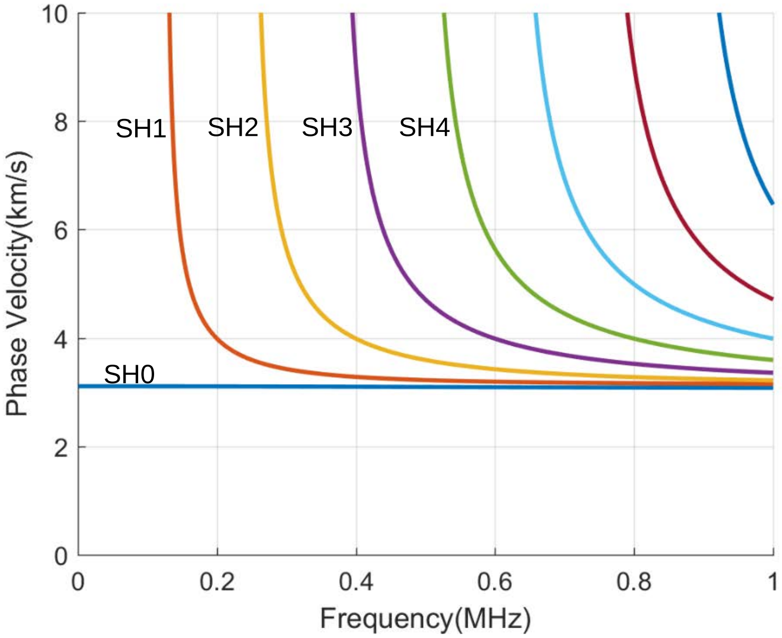

Figure 16: Shear Horizontal Wave Phase Velocity Dispersion Curves for the 24-inch steel pipe with 0.5-inch wall

3.1.6 24-inch cast iron pipe with 0.5-inch wall

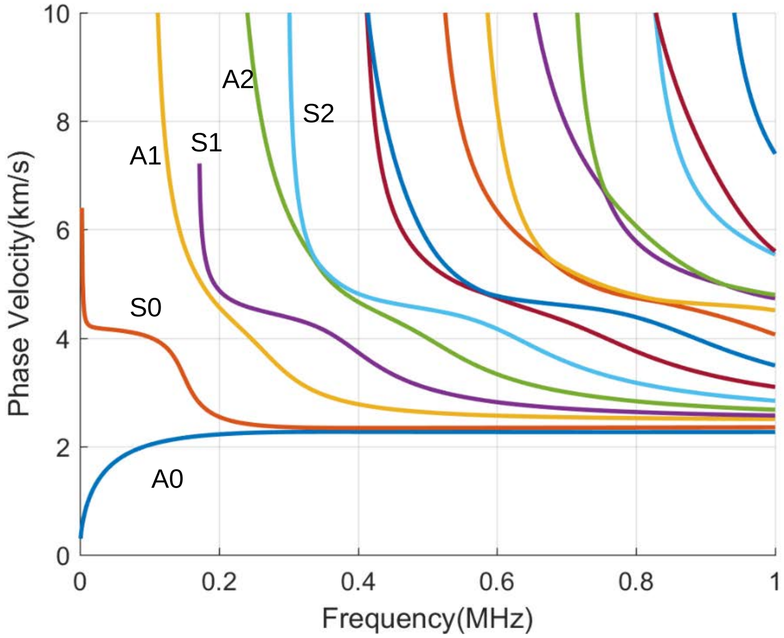

Figure 17: Lamb wave phase velocity dispersion curves for the 24-inch cast iron pipe with 0.5-inch wall

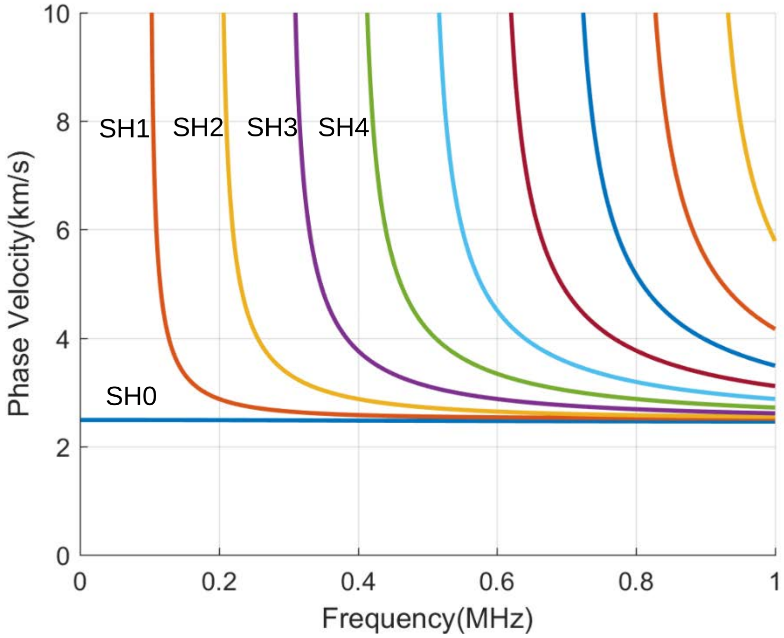

Figure 18: Shear horizontal wave phase velocity dispersion curves for the 24-inch cast iron pipe with 0.5-inch wall

3.1.7 Summary

To summarize the dispersion analysis, the following conclusions are drawn:

1. There are two major categories of guided wave modes namely Lamb wave and Shear Horizontal wave. They possess different vibration polarizations in isotropic materials like steel and cast iron and should be treated separately. The different natures of these modes also require different design of transducers.
2. For the same material, the thickness of the plate or pipe is the dominant factor that determines the dispersion curves.
3. In this work, the 12-inch and 24-inch OD pipes have similar dispersion curves as a flat plate as long as they are of the same thickness. As shown in Figure 19 and Figure 20, the phase velocity and group velocity dispersion curves for these three structures are plotted together, and they are very close to each other. As a result, it is helpful to test wave excitation and propagation on the flat plate since the flat plate is much easier to handle than the interior of the pipe. The results can be readily transferred to the sensor design for the pipe.

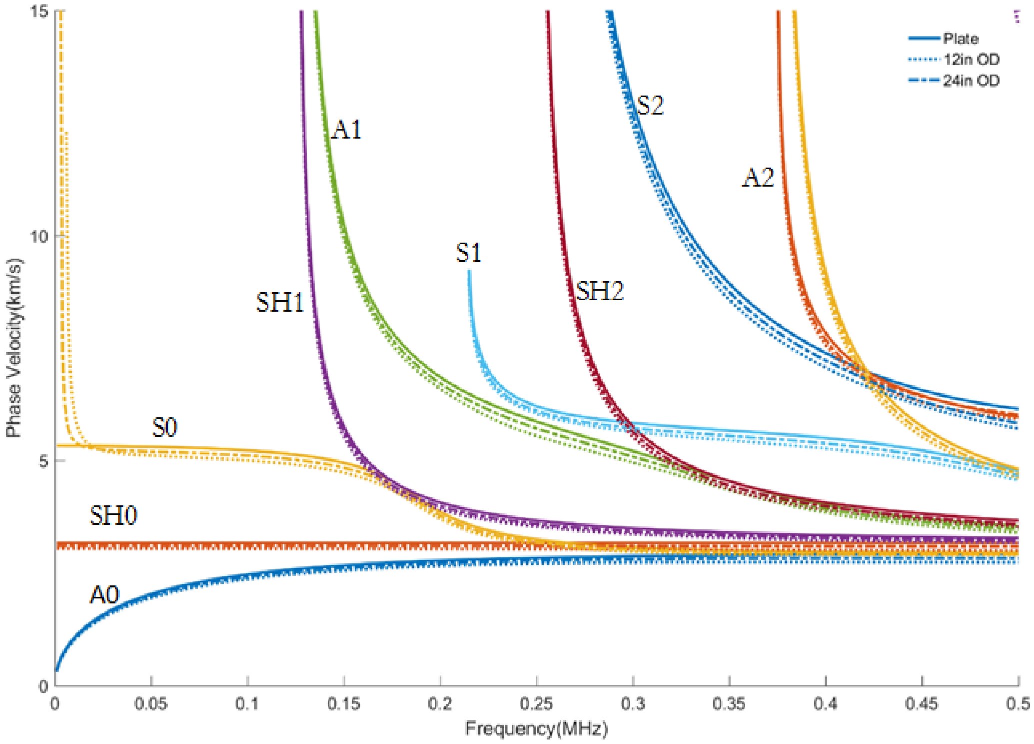

Figure 19. Phase velocity dispersion curves of both Lamb and SH wave modes for the flat plate (solid line), 12-in pipe (dotted line) and 24-in pipe (dot-dash line).

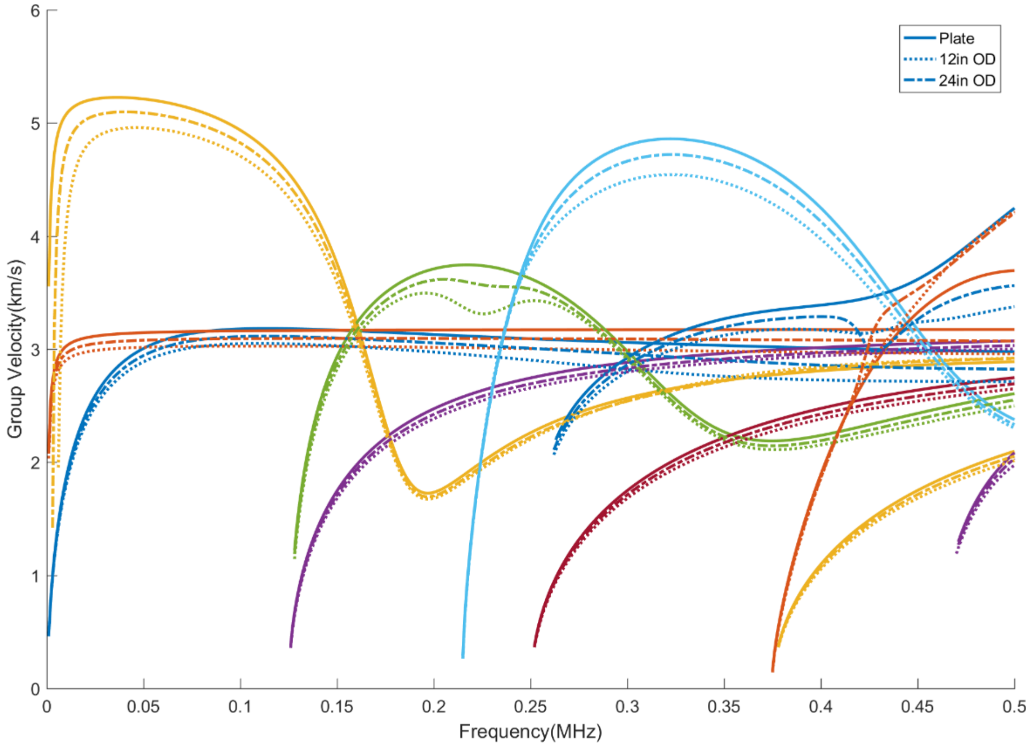

Figure 20. Group velocity dispersion curves of both Lamb and SH wave modes for the flat plate (solid line), 12-in pipe (dotted line) and 24-in pipe (dot-dash line).

3.2 Selecting Excitation Mode

The dispersion curves shown in 3.1 provides all the possibilities of propagating guided wave modes existing in the structure of interest. Every point on the dispersion curves is a possible excitation point. The excitation mode is thus defined as a frequency-mode combination. Since there are so many excitation modes and they have different propagation characteristics, the optimal excitation mode has to be selected.

To select optimal excitation modes for inspection, the following guidelines are followed

1. The mode should have relatively low dispersion at the frequency range of interest such that its wave packet does not spread and attenuate too fast. A low dispersive region is where the phase and group velocity do not change a lot with frequency.
2. The excitation point should be isolated from other wave modes such that the excitation does not excite multiple modes simultaneously. If multi-mode excitation is practically inevitable, the desired wave mode should be the dominant one.

It should be noted that the above criteria only take into account the wave propagation characteristic but do not consider the sensitivity to the defects. The sensitivity to the defect can be either be predicted by finite element simulation or studied through experiments. In this project, ULC employed the experimental method as the primary tool but also utilized finite element model for validation.

4 PLATE TEST

The testing in this phase was focused on experimentally evaluating the usefulness of all the candidate wave modes, developing plate wave propagation models using Finite Element Analysis (FEA) using a baseline set of assumptions, and testing plates to validate the models. The effort also involved performing sensor design, fabrication, testing, and evaluation to develop approximate design parameters that would be used for subsequent pipe testing. Testing with plates reduces the wave propagation problem to that of 1-Dimensional (1D) resulting in a simpler analysis for selection of the coil and magnet and a simpler means for evaluating ultrasonic wave properties and sensor performance. Knowledge acquired by testing EMAT guided wave in plates is a valuable prerequisite to pipe test as it can be used to simplify the testing and evaluation of pipes.

4.1 Evaluation of Excited Waves (Group Velocity Matching and Single Dominating Mode):

In this section, to explain the evaluation of guided wave excitation, the 0.25-inch plate has been taken as an example.

Figure 21 shows the phase velocity dispersion curves for the Lamb wave modes for the 0.25-inch steel plate. The red lines (dashed) correspond to different wavelengths that are characteristic of the coils in the EMAT sensor test kit collection. The colored curves in Figure 21 are the phase velocities of different wave modes that can be generated in the material.

The intersections of the red dashed lines, and the phase velocity curves are marked as yellow dots, and each one has been numbered. These points pertain to the wave modes that can be excited in the material with the set of coils available in the kit.

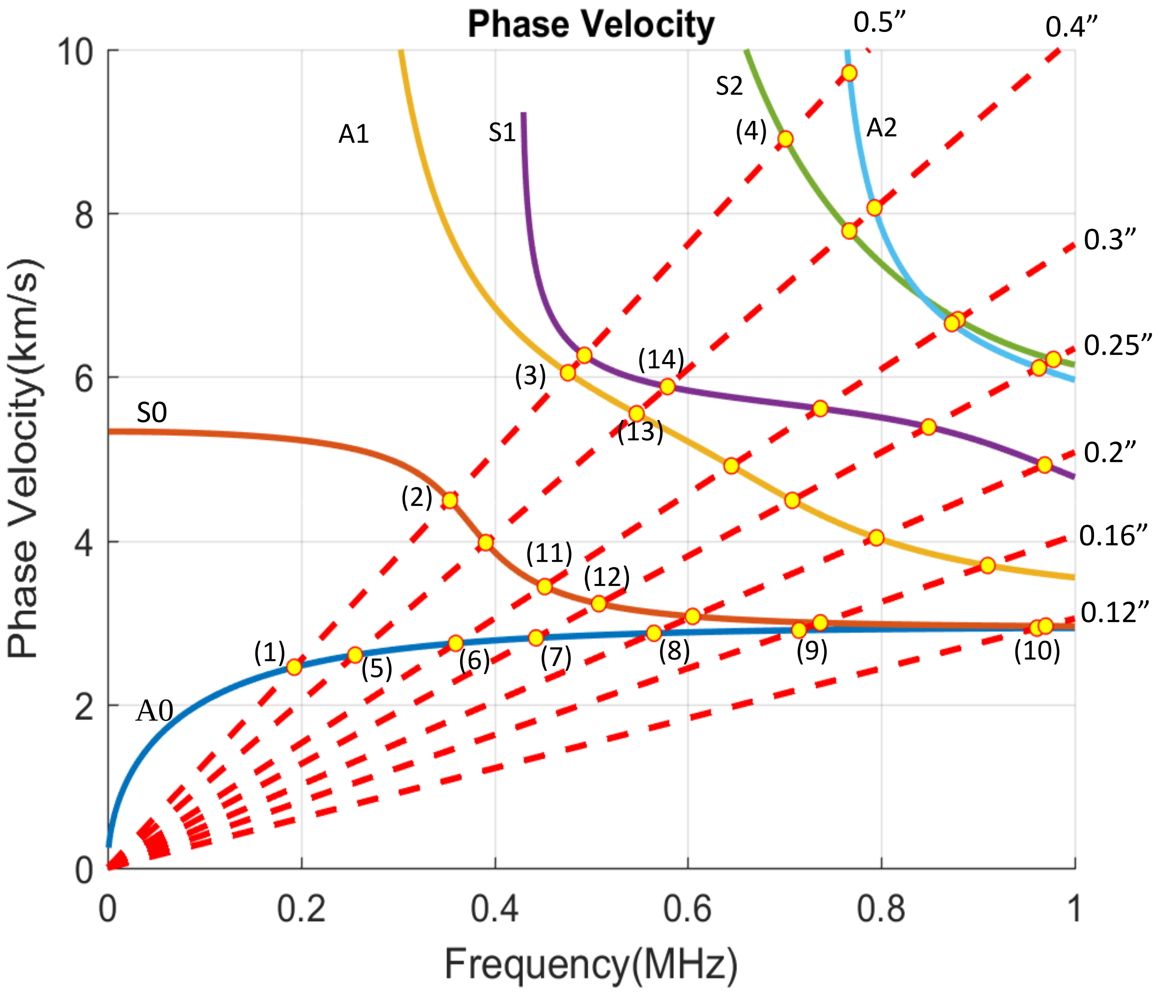

Figure 21: Lamb Wave Phase Velocity Curves for 0.25-inch Steel Plate and Excitation Points

The yellow excitation points have been overlaid on group velocity dispersion curves shown in Figure 22 to assist with the group velocity matching. By reviewing the group velocity curve the amount of dispersion for each excitation point and the excitation of single dominant mode was evaluated, and the most optimal excitation points were determined. The objective of the EMAT design step was to come up with the optimal center frequency and coil spacing (spacing between adjacent wires).

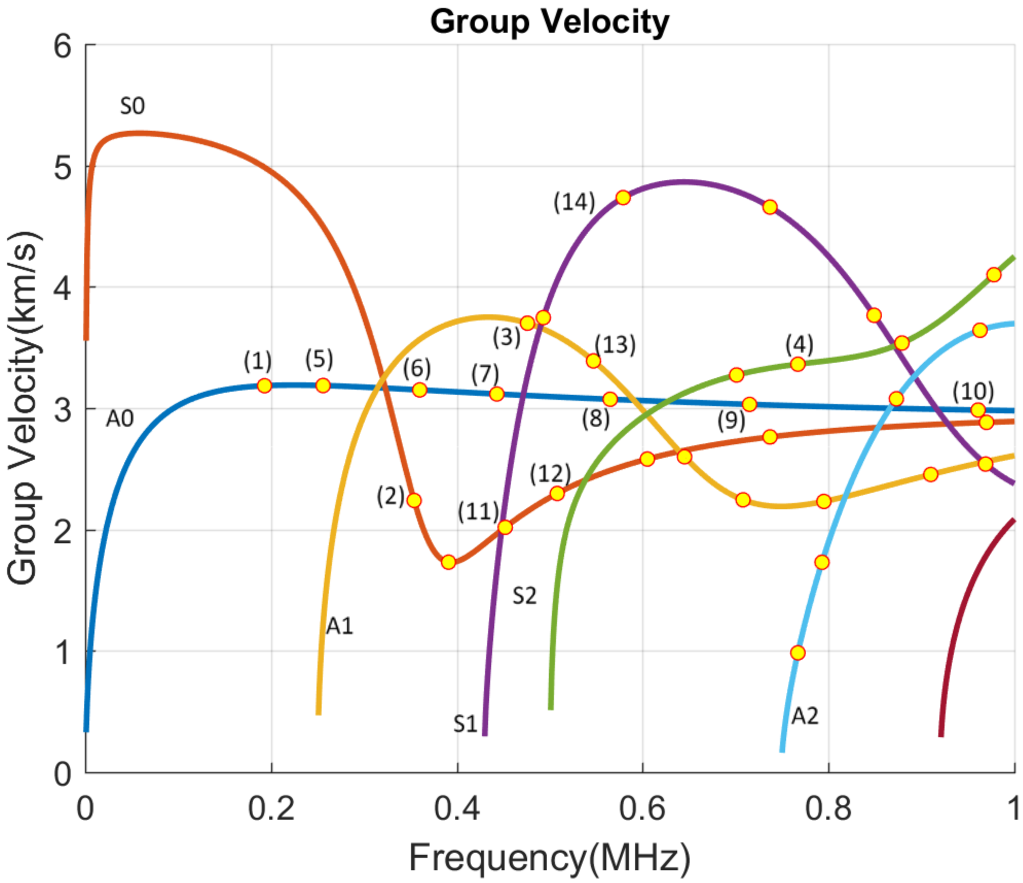

Figure 22: The Group Velocity Dispersion Curves for the Lamb Wave Modes Existing in a Quarter-inch Steel Plate

4.2 Material Dependence and Liftoff Effect

4.2.1 Material Dependence

Steel and cast iron are common materials used in pipes. The material properties of both are different which results in different efficiencies of EMAT wave excitation. This “Material Dependence” part of the study was performed to evaluate the wave amplitudes that can be excited in steel and cast iron and to quantitatively compare these amplitudes.

The dispersion curves of a quarter inch thick cast iron plate were calculated using MATLAB and plotted in Figure 23.

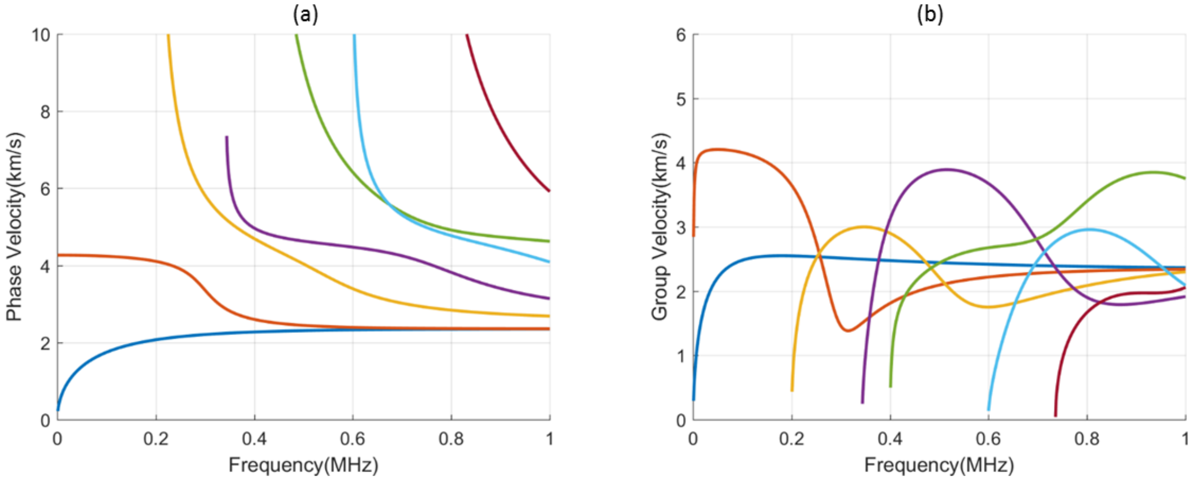

Figure 23: Dispersion Curves of a Quarter-inch Thick Cast Iron Plate: (a) Phase Velocity and (b) Group Velocity

The steel and cast iron plates for testing were chosen to be of the same thickness. For a comparative study, the same thickness allows us to control the experiment so that only the effect of the material properties are witnessed. It was seen (from the phase velocity curves) that the steel plate has higher phase velocity than the cast iron plate at all frequencies.

4.2.2 Liftoff Effect

The liftoff of the Tx and Rx have a significant effect on the intensity of wave amplitude and should always be kept as small as possible. A smaller liftoff results in higher wave intensity which can produce a good signal-to-noise ratio and increase the wave propagation distance. However, in actual field applications, a sensor with a liftoff too small may be vulnerable to interaction with debris or uneven surface of the pipe surface and could be damaged by the pipe's surface roughness. Thus, it is desirable to hit a balance between the signal-to-noise ratio and vulnerability to surface condition.

In this test, plastic shims of varying thickness were inserted between the EMAT and the steel plate to give different liftoffs. The liftoff values that were produced by combining different plastic shims were 0.7mm, 1.6mm, 1.8mm and 2.3mm. The liftoffs of the Tx and the Rx were kept the same. The maximum amplitude vs. liftoff is plotted in Figure 24. It was observed that the wave amplitude decreases when liftoff increases. Also, it was observed that the amplitude drops quickly when the liftoff is over 1.6mm. For the current setup, the 1.6mm liftoff gave a good clearance without compromising too much excitation power and was selected as an optimal point.

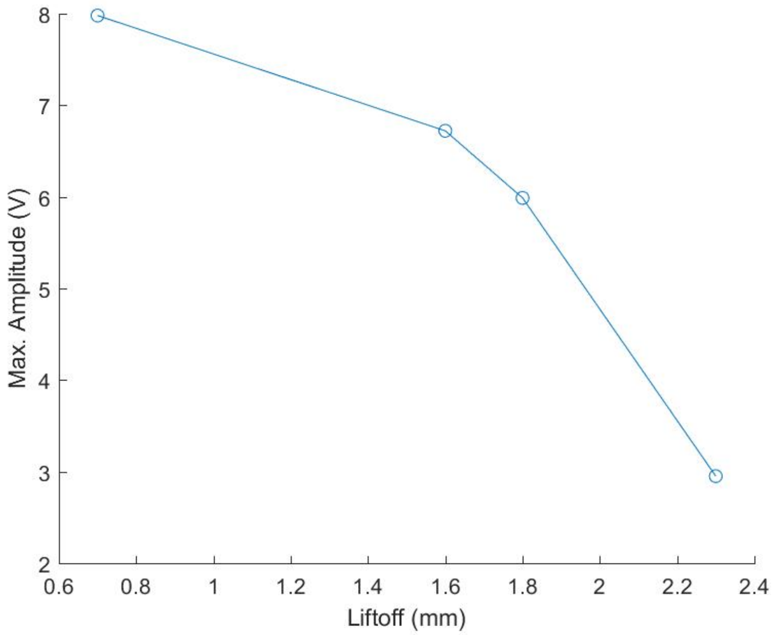

Figure 24: Maximum Amplitude vs. Liftoff Plot

4.3 Wave Propagation

Waves propagating in any media are subject to attenuation. Attenuation can be the resultant of multiple factors. For the waves in plates, these factors include wave dispersion, beam divergence, and the presence of coatings or attached soils. In practice, it is crucial to choose waves with low attenuation to maximize the propagation distance, increase coverage area and maintain a desirable signal-to-noise ratio.

In addition to attenuation, beam divergence is also critical when selecting waves since it also affects the signal intensity at the desired inspection location, the coverage region of inspection, and the signal-to-noise ratio.

The testing was performed to evaluate the following:

1. The wave magnitude attenuation for an on-axis receiver at different propagating distances, and
2. The distribution of wave energy due to beam divergence by positioning the receiver at different off-axis locations.

4.3.1 Attenuation

Wave amplitude attenuation is a combined result of material damping, wave dispersion, and beam divergence. The material damping here is exclusively due to the viscoelasticity of material. The material damping of steel is usually very low and is assumed to be negligible in this study. The attenuation studied here is mainly the result of wave dispersion and beam divergence. Measurements were made along the steel plate and are shown in Figure 25(a).

In parallel, an FEA was conducted to simulate the wave propagation. The dimensions used in the FEA model are exactly the same as those in the experiment. The results of the FEA simulation are shown in Figure 25(b). Since the signal voltage is not available in the FEA model the longitudinal in-plane displacement in the x-direction is used instead. The results show that the amplitude at the farthest distance from the Tx decreased more than 50% of that measured at the nearest distance from the Tx, over the total propagation distance. It is observed that the amplitude decreases faster at the short propagation distance and slower at the long distance. The amplitude decrease is expected to be even slower for the propagation distance longer than 900 mm.

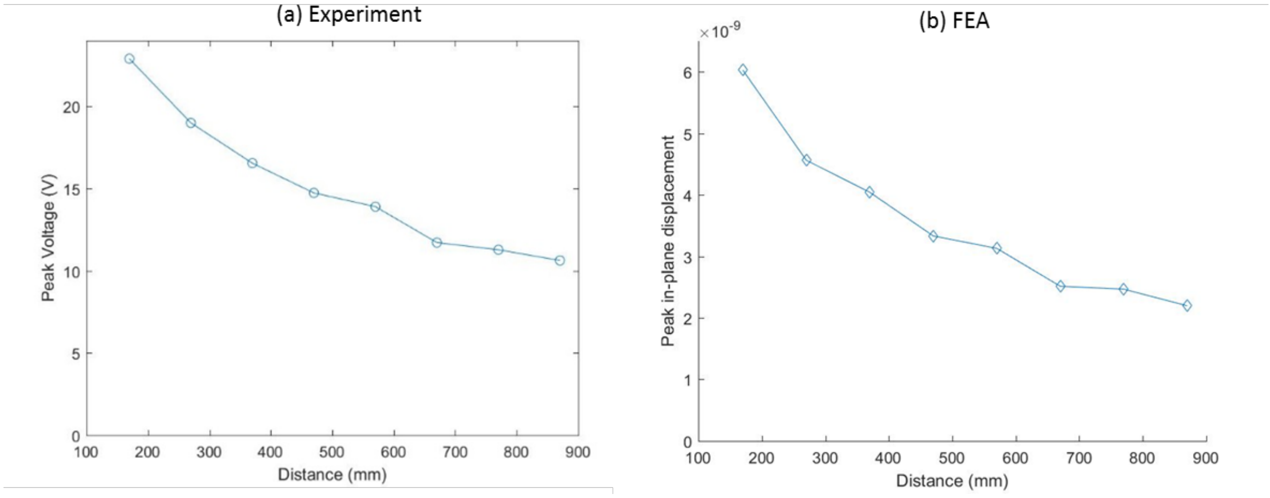

Figure 25: The Amplitude Change for On-axis Receiver. (a) Experimental Result (b) FEA Simulation Result

The two amplitude plots were normalized by their mean values respectively and plotted in Figure 26. The trends of the two results agree very well which confirms the validity of the FEA model.

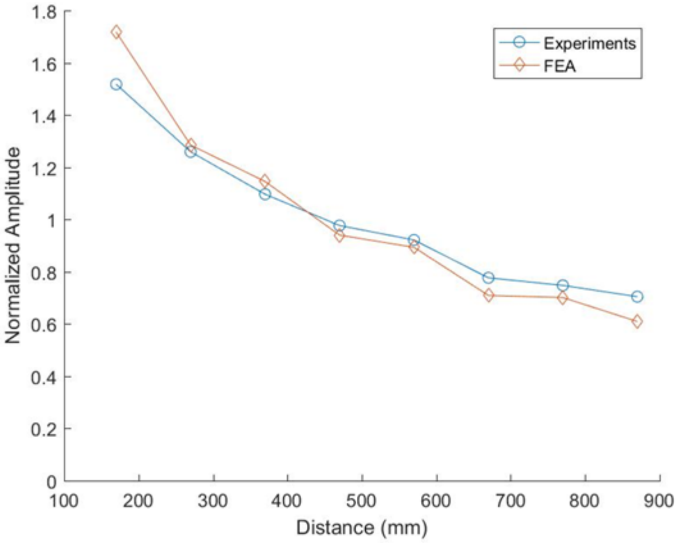

Figure 26: The Comparison between Normalized Experiment and FEA Results

4.3.2 Beam Divergence

To gain more insight into the wave propagation in a plate, the study of the distribution of wave field due to beam divergence was conducted.

The peak amplitude of the A-scan signal is taken as the wave magnitude. The wave magnitude at different locations is plotted as a contour plot for experiment and FEA results respectively in Figure 27. It is observed that the distribution of the two results is similar. The color intensity indicates the maximum amplitude received at different locations. The units of the color intensity are “volts” and “meters” for the experiment and FEA results respectively. The wave beam becomes very wide after a certain distance of propagation.

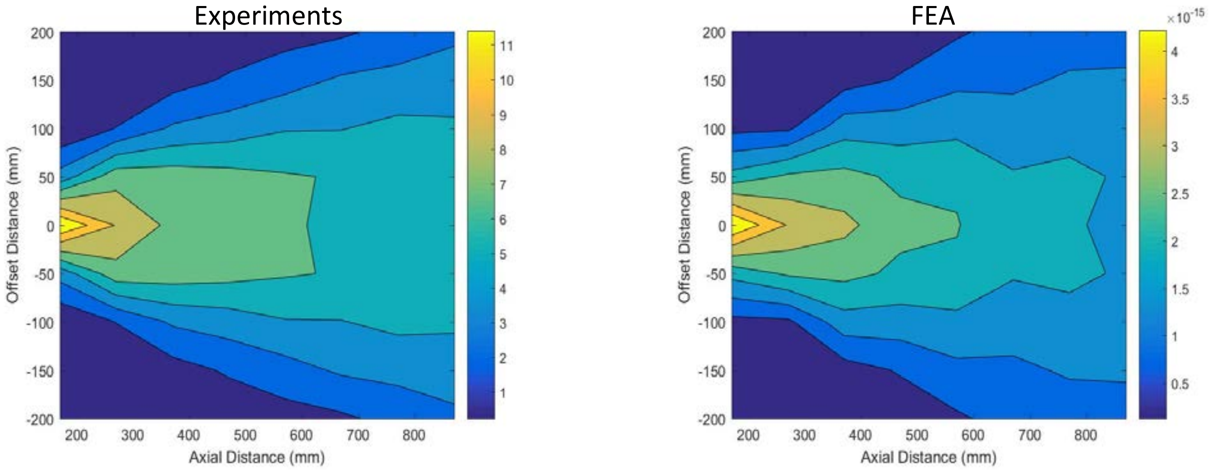

Figure 27: Lamb Wave Fields for Beam Divergence Study: Experiment (left) and FEA results (right)

The beam divergence angle is defined as the angle between the -6 dB amplitude line and 0 dB amplitude line illustrated in Figure 28. Since the wave is also attenuated in the 0 dB line for different propagation distance, the amplitudes are normalized for each x location. The difference between the two divergence angles is 0.8° or 5.5% relatively which is very small. The agreement between the experiments and the FEA result is good, and the FEA can be used to study the beam divergence of any other case.

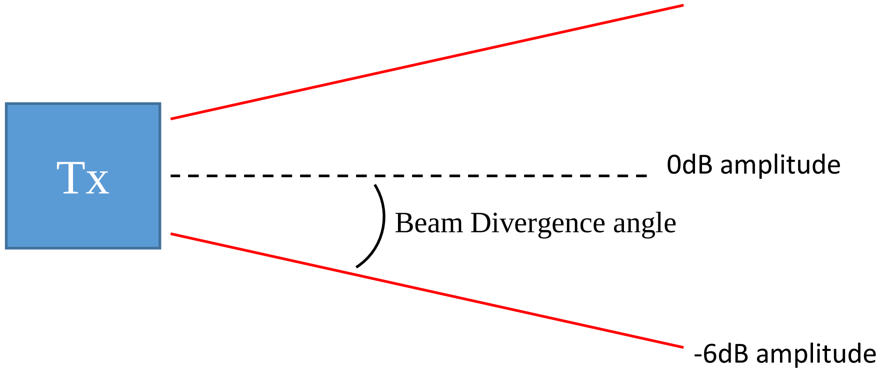

Figure 28: Sketch Shows the Definition of Beam Divergence Angle

4.4 Summary

In the plate test, multiple characteristics of guided wave excitation and propagation have been studied.

1. The fact that experimentally measured group velocities match the predicted group velocities verifies the calculation of dispersion curves as well as the successful excitation of desired wave modes.
2. It has been found that the cast iron material in nowadays is as good as carbon steel in terms of its use as an ultrasonic waveguide.
3. The increase in liftoff could decrease the wave amplitude significantly.
4. The wave attenuation along the propagation distance was studied. The FEA produces accurate amplitude reduction along the propagation distance.
5. The wave beam divergence was also studied and verified through FEA. Due to beam divergence, the beam width increases as the wave propagates. For long propagation distance, the diverged wave may interact with defects or edges that are not on the straight path from Tx to Rx.

5 EMAT DESIGN

The design parameters of EMAT were studied with the intent of being able to design and build miniature, curve-adapting EMATs for inner pipe surfaces.

5.1 Design of EMATs

ULC custom designed and made prototype EMATs. The sensors were placed on the quarter-inch steel plate, and a side-by-side comparison with off-the-shelf EMATs was made.

In the EMAT design part of the evaluation, customized EMATs were prototyped and demonstrated to be working properly which verifies our understanding of the transduction mechanism of EMAT. Through successive design iterations, a robust EMAT housing was developed which is shown in Figure 29.

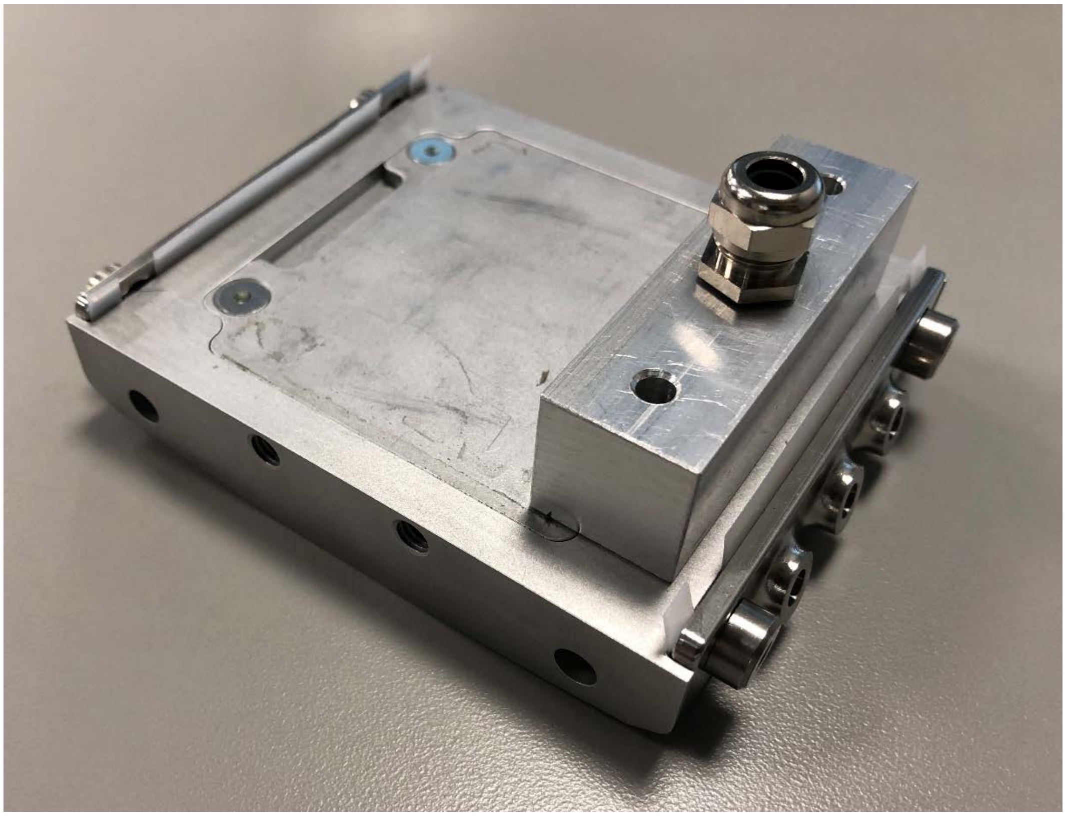

Figure 29. A photo of the final design of the EMAT prototype with aluminum housing.

5.2 Summary

ULC prototyped and tested EMATs. The 3D-printed housing with magnets and coil has been demonstrated to successfully excite the desired wave modes. Later, aluminum housings were used to replace the 3D-printed housing and also gave good results. The housing has been improved through several iterations to increase its stiffness and robustness and reduce the friction.

6 PIPE TEST

Pipe testing covered different pipe diameters, different materials and different manufacturing processes, i.e., seamless vs. ERW. It employed a motor-driven test bench which guarantees the high accuracy and resolution during the scanning. Multiple wave modes were tested for their performance in pipe inspection. Several types of defects with different sizes were inspected using the EMAT guided wave technique.

6.1 Test setup

The following describes some examples of the test setup.

6.1.1 12-inch seamless steel pipe with artificial defects

The pipe test bench has a total length of 62,” but since there are fixtures near the two ends of the pipe, only 50” of the pipe can be scanned. Four types of artificial defects were created at the 12 o’clock position across the 50” length and are shown in Figure 30 as longitudinal notch, thinning, circumferential notch, and through-hole. The exact locations of these defects are listed in Table 3. Also, the sizes of artificial defects and corresponding labels are shown in Table 3. The labels are used in the data post-processing description to refer to these different defects. The origin is set at 6.907 inches from one end of the pipe.

A servo motor was used to drive a center plate (inside the pipe) in the pipe axial direction. Two EMATs are attached to the center plate and are located circumferentially at fixed positions 90° apart, as shown in Figure 31. The nominal position is where the Transmitter (Tx) and Receiver (Rx) are equally spaced on either side of the 12 o’clock position. At this position, the A-scan signal was collected every 1 mm during the scanning, and 1270 A-scan signals were obtained during a single scan.

The center plate was then rotated in 15° increments such that the Tx and Rx remained 90° apart but ended up in different clock positions, and the A-scan signals were obtained for each incremental rotation. In this manner, the A-scan signal was collected for a total of 360°/15°=24 positions. This procedure was followed to simulate conditions in which a defect may appear at any clock position.

For each clock position, the scan was conducted for the 50-in length for SH0 and SH1 modes separately. Therefore, a total of 48 scans were obtained.

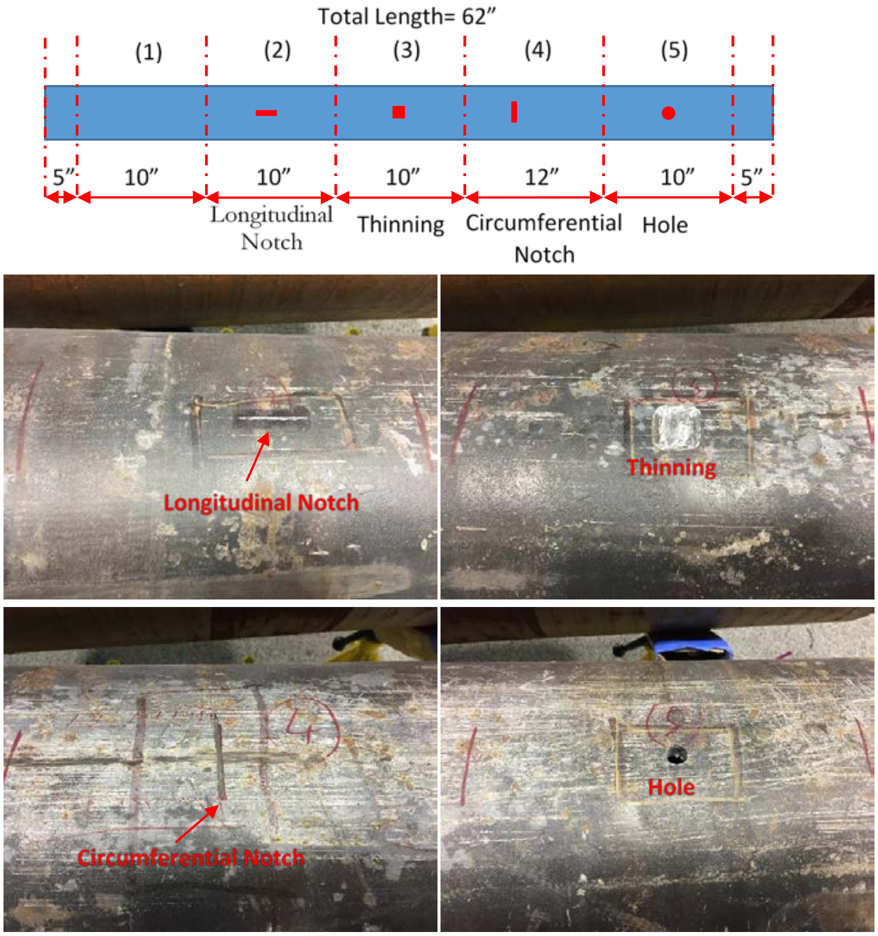

Figure 30. Locations of defects on the 12-in pipe and photos of different defects.

Table 3. Dimensions and locations of artificial defects on the 12-inch seamless steel pipe

Type	Size	Location	Circumferential location
Longitudinal Notch (LNotch)	Length: 1 inch Depth: 0.1 inch	35.09”	12:00
Wall Thinning (Thinning)	Length: 1 inch Width: 1 inch Depth: 0.1 inch	25.59”	12:00
Circumferential Notch (CNotch)	Length: 2 inch Depth: 0.1 inch	16.09”	12:00
Through Hole (Hole)	Diameter: 0.5 inch	3.09”	12:00

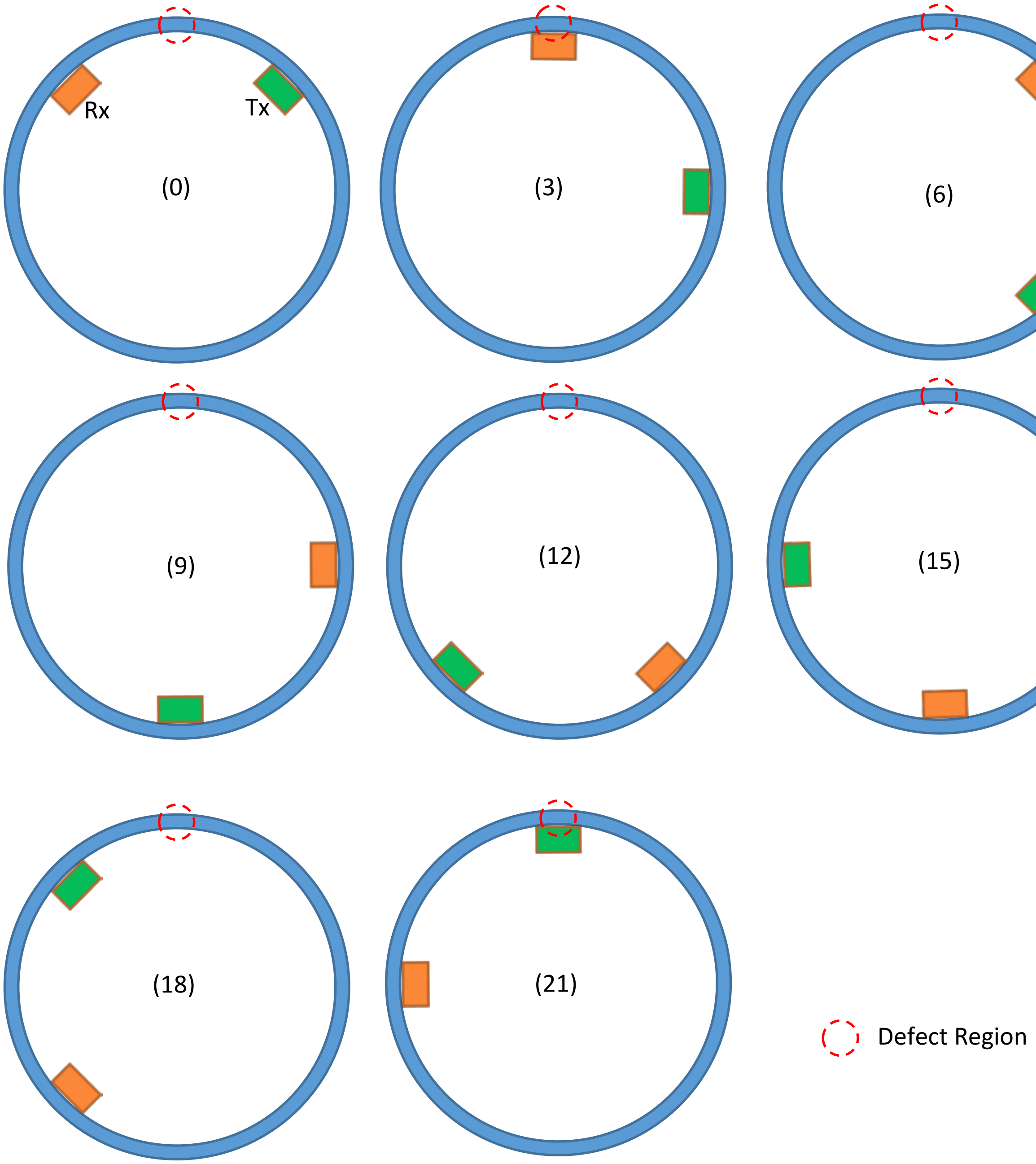

Figure 31. Different defect clock positions relative to Tx and Rx.

6.1.2 24-inch seamless steel pipe with artificial defects

The test bench was modified to fit the 24-inch pipe as shown in Figure 32.

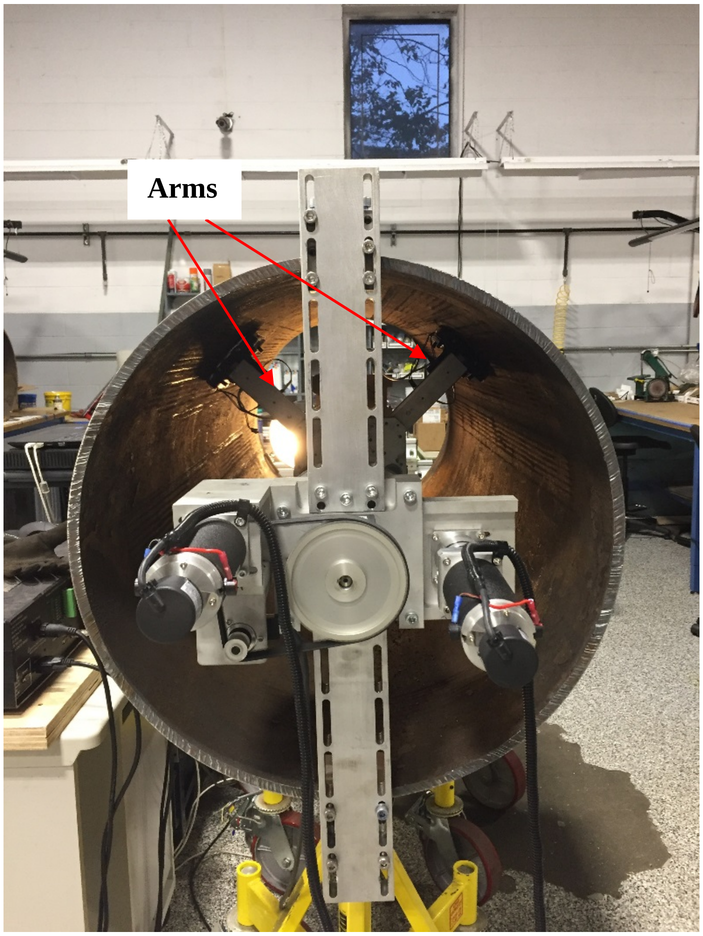

Figure 32. The test bench for 24-inch steel pipe.

Table 4. Dimensions and locations of artificial defects on the 24-inch seamless steel pipe

Type	Size	Axial location	Circumferential location
Longitudinal Notch 1	Length: 1 inch Depth: 0.1 inch (20% thickness)	20.00”	12:00
Longitudinal Notch 2	Length: 1 inch Depth: 0.05 inch (10% thickness)	14.25”	3:00
Longitudinal Notch 3	Length: 1 inch Depth: 0.1 inch (20% thickness)	24.25”	3:00
Local Wall Thinning	Length: 1 inch, Width: 1 inch Depth: 0.1 inch (20% thickness)	40.00”	12:00

6.1.3 24-inch ERW steel pipe with artificial defects

A 24-inch ERW pipe was also used for the pipe test. It has the same pipe geometry, i.e., diameter and wall thickness, as the 24-inch seamless pipe except it is manufactured through ERW method. The welding line is shown in Figure 33. The inner surface of the welding line has quite a smooth surface. This is beneficial to guided wave propagation since it will not introduce numerous reflections. Also, the ERW pipe is manufactured by welding flat steel plate; it is expected the inner surface is more uniform than the seamless pipe because the steel plate thickness is usually controlled to a very accurate level. As listed in Table 5, three longitudinal notches are induced on the welding line; three longitudinal notches are induced on the regular pipe walls and four local wall thinning are induced on the regular pipe wall. The welding line is at the 12:00 position.

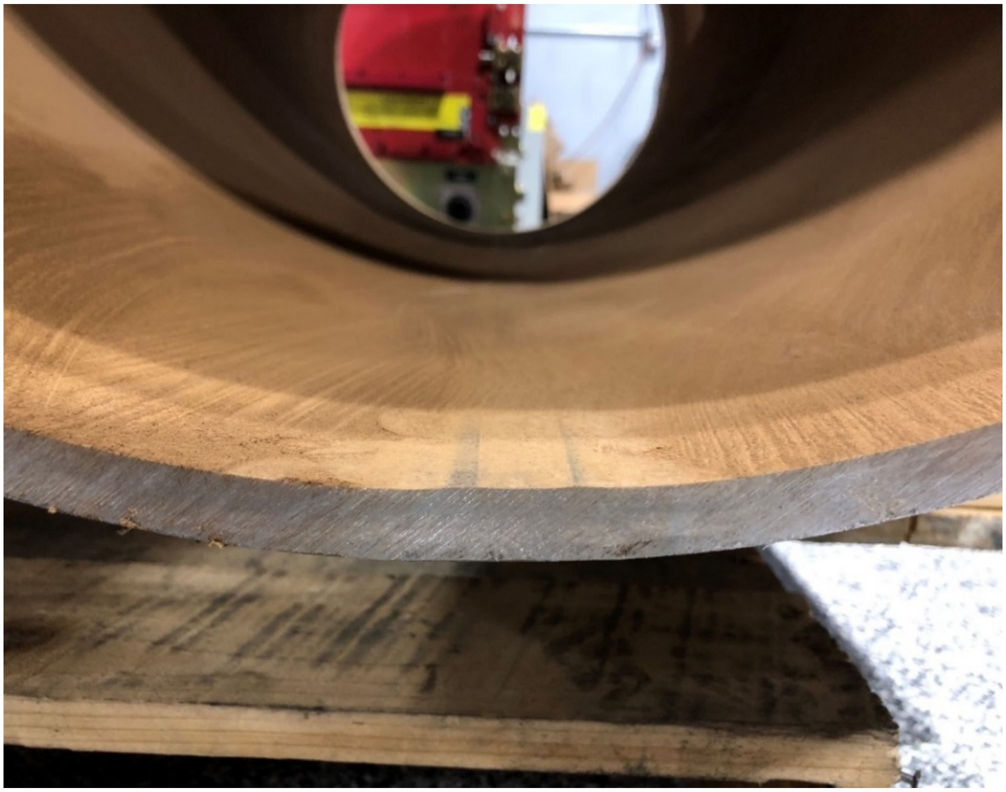

Figure 33. A photo shows the welding line of the 24-inch ERW pipe

Figure 34. A photo shows the 24-inch ERW pipe with the local wall thinning defects facing to the front.

Table 5. Dimensions and locations of artificial defects on the 24-inch ERW steel pipe

Type	Size (unit: inch)	Axial location (unit inch)	Circumferential location
Longitudinal Notch 1	Length: 1 Depth: 0.05	15	3:00
Longitudinal Notch 2	Length: 1 Depth: 0.1	25	3:00

Type	Size (unit: inch)	Axial location (unit inch)	Circumferential location
Longitudinal Notch 3	Length: 1 Depth: 0.15	35	3:00
Longitudinal Notch 4 (on the weld)	Length: 1 Depth: 0.05	20	12:00
Longitudinal Notch 5 (on the weld)	Length: 1 Depth: 0.1	30	12:00
Longitudinal Notch 6 (on the weld)	Length: 1 Depth: 0.15	40	12:00
Local Wall Thinning 1	Length: 1 Width: 1 Depth: 0.05	15	9:00
Local Wall Thinning 2	Length: 1 Width: 1 Depth: 0.1	25	9:00
Local Wall Thinning 3	Length: 1 Width: 2 Depth: 0.1	35	9:00
Local Wall Thinning 4	Length: 2 Width: 1 Depth: 0.1	45	9:00

6.1.4 24-inch cast iron pipe with artificial defects

Cast iron pipe is another important material to consider when studying guided wave interaction with defects in metal pipes. The size and locations of the defects are shown in Table 6. It is worth mentioning that cast-iron pipe is usually not operated under high pressure. Also, cast-iron is relatively brittle compared with carbon steel due to its high carbon content and is thus not as fatigue-resistant as steel. As a result, fatigue cracks are not commonly seen on cast iron pipe and were not studied in this test.

.

Table 6. Dimensions and locations of artificial defects on the 24-inch cast iron pipe

Type	Size (unit: inch)	Axial location (unit inch)	Circumferential location
Local Wall Thinning 1	Length: 1 Width: 1 Depth: 0.05	15	9:00
Local Wall Thinning 2	Length: 1 Width: 1 Depth: 0.1	25	9:00
Local Wall Thinning 3	Length: 1 Width: 1 Depth: 0.15	35	9:00

6.2 A-scan signal amplitude and B-scan

Before getting to the test results, two fundamental ways of representing the wave signal, namely A-scan and B-scan are introduced here.

The A-scan signal is the raw waveform collected from 0 to 1500 μs with a sampling frequency of 10 MHz. An example is shown in Figure 35. Figure 35 (a) and (b) show the raw waveform and wave amplitude respectively of an A-scan signal taken at d=10.09 inch when the Tx and Rx are placed at position 1.

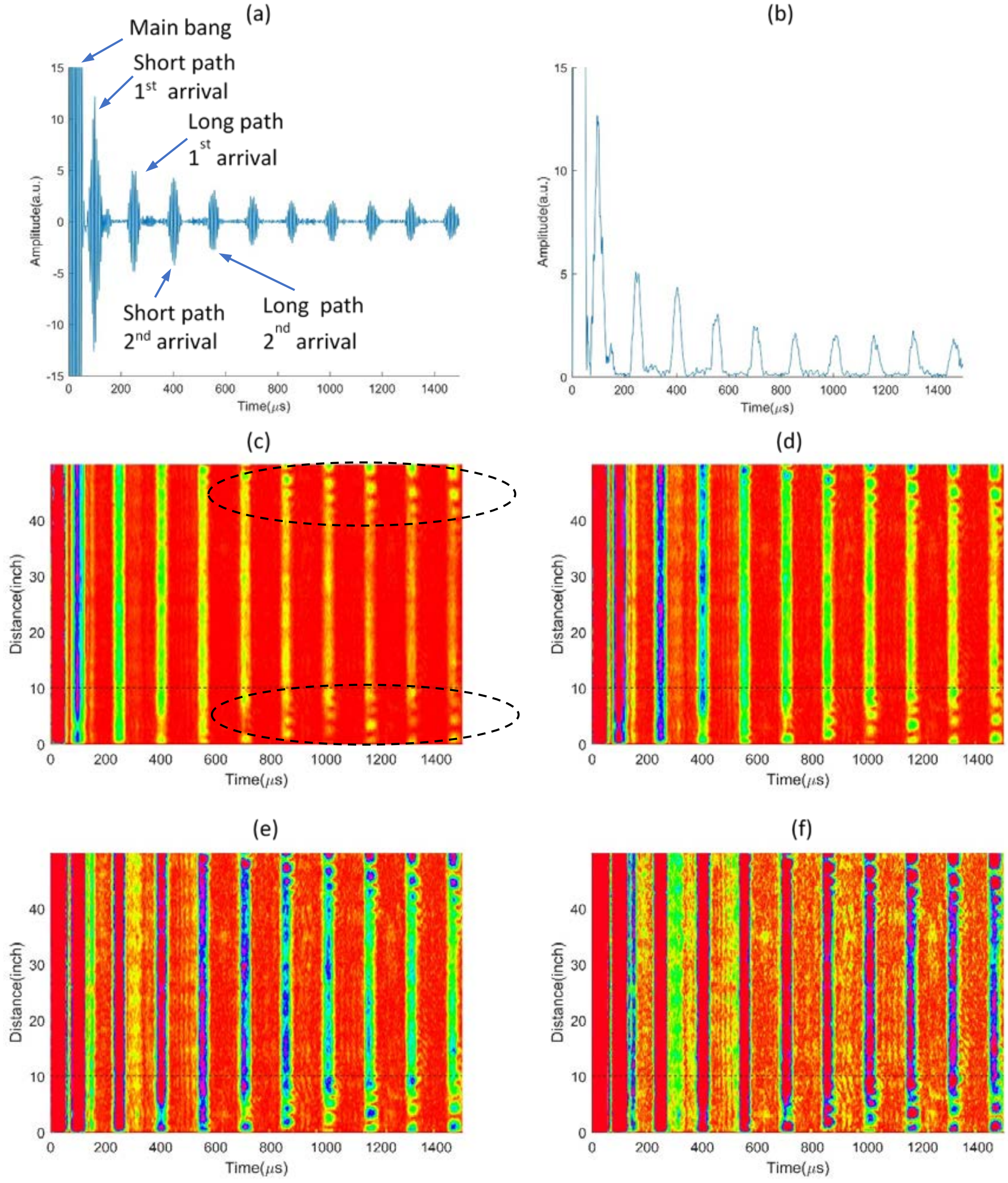

Figure 35. A-scan results and B-Scan results with different color intensity maps.

The very strong signal received at t=0 is the main bang (or dead zone). Main bang is a large signal in the receiver output created by the transmitter pulse. This is such a large signal that it completely overloads the receiver, preventing it from detecting any reflections during this time. The duration of the main bang includes the length of the transmit pulse, and a period of time immediately after transmitting, during which the transmit pulse decays to a level small enough so that it no longer interferes with the detection of reflections. The main bang arises due to the interference between the pulser circuit and receiver circuit.

The wave packets following the main bang are the ultrasonic wave signals. The Tx transmits two wave packets of the same wave mode that propagate in opposite directions such that one travels clockwise and the other travels counter-clockwise. Since the Tx and Rx are 90° apart, the first wave packet labeled "short path 1st arrival" is the 1st wave arriving through the short path traveling through 90°. Then, the 2nd wave packet arrives through the long path which travels 270° and is labeled as "long path 1st arrival". Since the circumference of the pipe provides a loop path for the guided waves, both the wave packets continue to travel after their 1st arrivals. The short path wave travels another 360° after its 1st arrival and arrives at the Rx again with a total traveling distance of 90°+360°=450°. This is labeled as "short path 2nd arrival". Similarly, the wave packet labeled as "long path 2nd arrival" has traveled totally 630° to arrive at the Rx for the 2nd time. All of the successive wave packets can be explained following this logic.

The wave amplitude is calculated through the Hilbert transform and plotted in Figure 5(b). It is noted that the amplitude of the wave packets attenuates quickly in the first few arrivals. This is due to the beam divergence. After the guided wave is transmitted by the Tx, the wave beam keeps spreading as it propagates.

By stacking all the amplitude plots for each A-scan signal collected every 1mm of axial displacement, i.e., Figure 5(b), into one plot and representing the amplitude as the color intensity, the B-scan plot is produced as shown in Figure 5(c). The B-scan and A-scan plots have the same x-axis. The vertical bands in B-scan plots correspond to different received wave packets. The color of the vertical bands indicates the amplitude of the wave packets. The x-axis is the time, and the y-axis is the axial distance between the EMAT starting point and ending point along the pipe axis (total 50" travel). If we assume the amplitude limit for Figure 5(b) isy_{max}, the limits for the color maps of Figures 5(c)-(f) are, y_{max}, $\frac{y_{max}}{2}$, $\frac{y_{max}}{4}$ and $\frac{y_{max}}{8}$ respectively. These limits are selected to improve the contrast such that damage feature can be easily seen. In Figure 5(c), it is clearly observed that there are interference patterns (interference of ultrasonic waves with a discontinuity) existing that are circled on the plot. Near the two ends of the pipe, the guided wave could hit the cut cross-section of the pipe and get reflected. The reflected wave will interfere with the circumferentially propagating waves and cause the amplitude to increase or decrease. The influence of such interference becomes more significant for longer traveling times because the reflected wave propagates away from the pipe end and toward the axial center of the pipe. Thus, in the lab experiments, the near-end region should not be used. Also, the time period for, data acquisition should be adjusted such that the measured time range is not affected by the interference signal. This interference patterns will also be generated by the two ends of each pipe section. So this data analysis method will be similar as that used for cast iron pipe inspection. However, for the welded steel pipes, each section of the pipe is much longer. For a long distance, this interference pattern will not be generated because no cross-section to reflect the circumferentially propagating guided wave. It may only happen near the welded zone because the weld itself could also reflect the guided wave, but this reflection will be weaker than the cross-section reflections. The B-Scan signal in the center region of steel pipe will not show the interference pattern, thus the data analysis will be simpler and the full measured time range can be used for the analysis. More details will be included in the following sections.

6.3 Determining the baseline signal

A baseline signal usually corresponds to the collective set of measurements made along a defect-free section of pipe. However, other factors may be present that could also influence the amplitude of signals along the section length such as liftoff change, uneven surface, and soil effects, and thus the baseline signal could vary within a certain range. This variation range should be considered as the generalized noise band within which the signal cannot be differentiated from defects. In other words, the defects could only be detected if the corresponding signal is significantly different from the baseline signal.

The average amplitude and standard deviation (STD or σ in the following content) is calculated and are plotted in Figure 36 (b). The $\pm 2\sigma$ noise band is also superimposed on the baseline mean plot. It is noted that the STD is large when a wave packet is received. This means the noise is not random noise since random noise will distribute evenly in time. High STD is caused by variations in ultrasonic guided wave during transmitting, propagating, and receiving which are affected by multiple factors mentioned before.

So far, the baseline signal is obtained with the statistical noise band. The next step is comparing the signals of known defects with the baseline signals.

Table 7. The coordinate ranges of the four baseline sections.

Baseline Section Index	Start (unit: inch)	End (unit: inch)
1	6.09	13.09
2	19.09	22.09
3	28.09	32.09
4	38.09	43.09

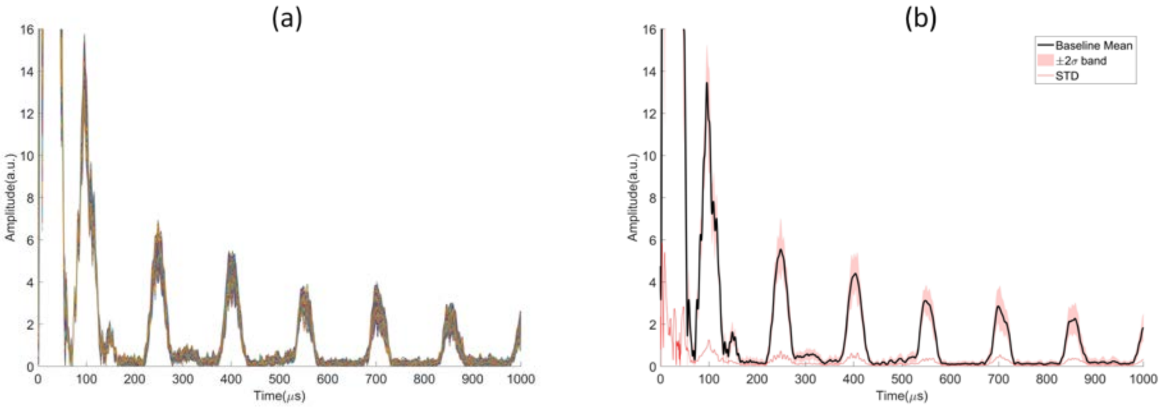

Figure 36. Baseline A-scan amplitude signals for (a) all 486 locations, and (b) mean amplitudes, noise band, and STD.

6.4 Defect signature: detection and classification

The defect detection is conducted by comparing an A-scan signal at a defect region with the corresponding baseline signals, i.e., mean signal and noise band as the EMATs travel axially over the defect region. If parts of the A-scan signal fall outside the noise band, which means the A-scan signal is either much stronger or much weaker than the baseline signals, there is a high possibility there are defects existing on the wave propagation path corresponding to this A-scan signal.

The through-hole is an unrealistic damage which only provides a reference to very severe damage. Longitudinal notch, circumferential notch and wall thinning simulate longitudinal crack-type defect, circumferential crack-type defect and corrosion defect respectively. Details of the defect detection of the longitudinal notch and wall thinning are presented in the following sections.

It is observed that the circumferential notch introduces minimal changes in A-scan signals and cannot be detected. By comparing the A-scan signals from artificial defects with the baseline signals, defect signatures to classify longitudinal notch and wall thinning have been determined.

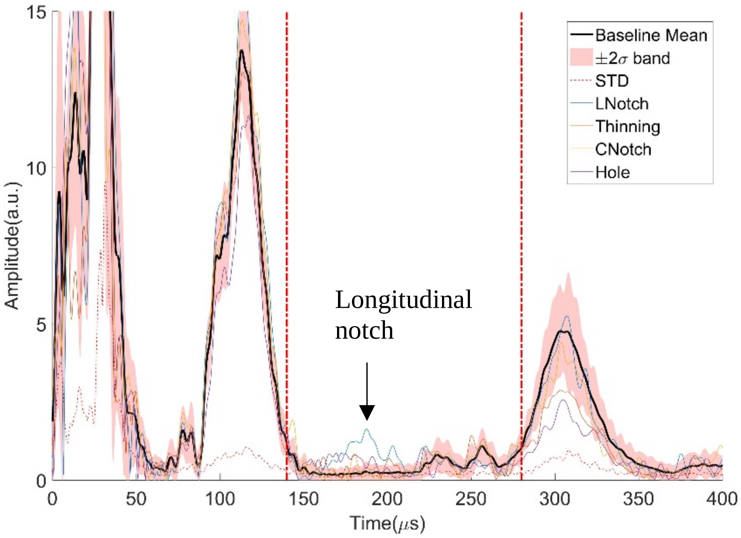

Figure 37. Sample A-scan signals collected at position 5 on the 12-inch pipe

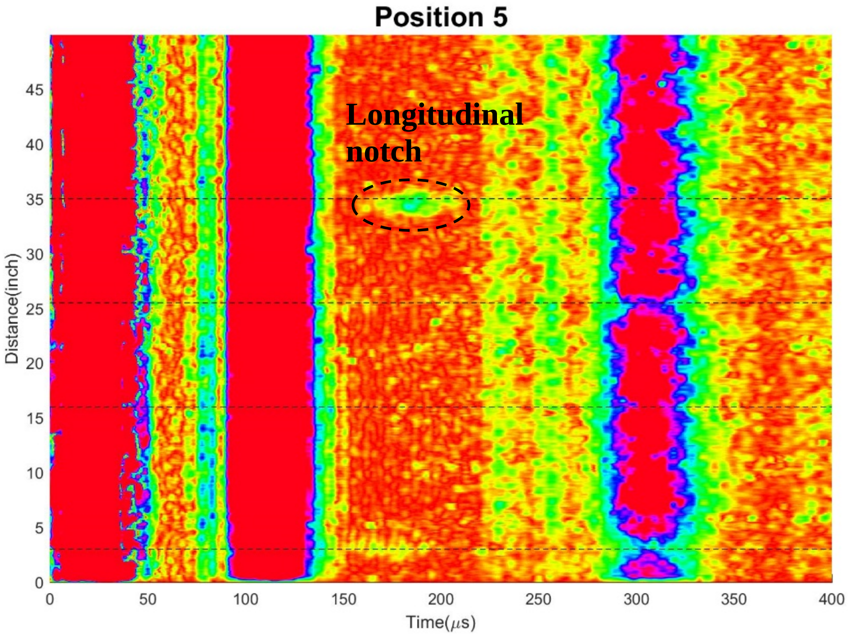

Figure 38. B-scan signals collected at position 5 on the 12-inch pipe

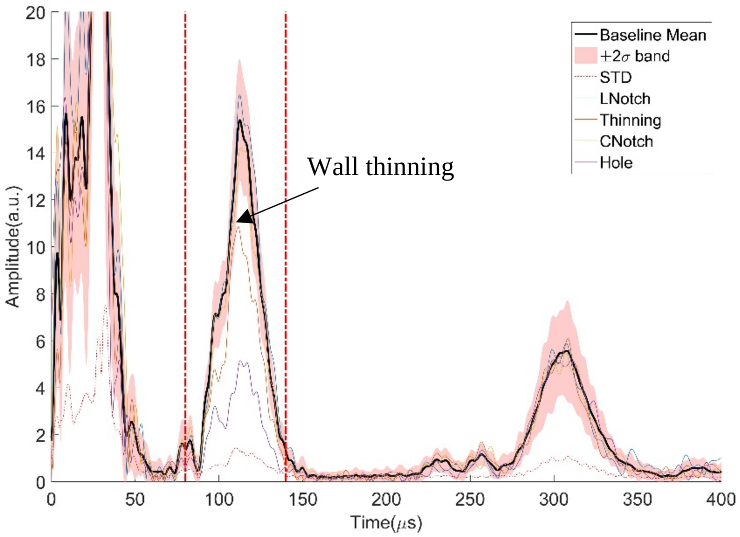

Figure 39. Sample A-scan signals collected at position 0 on the 12-inch pipe

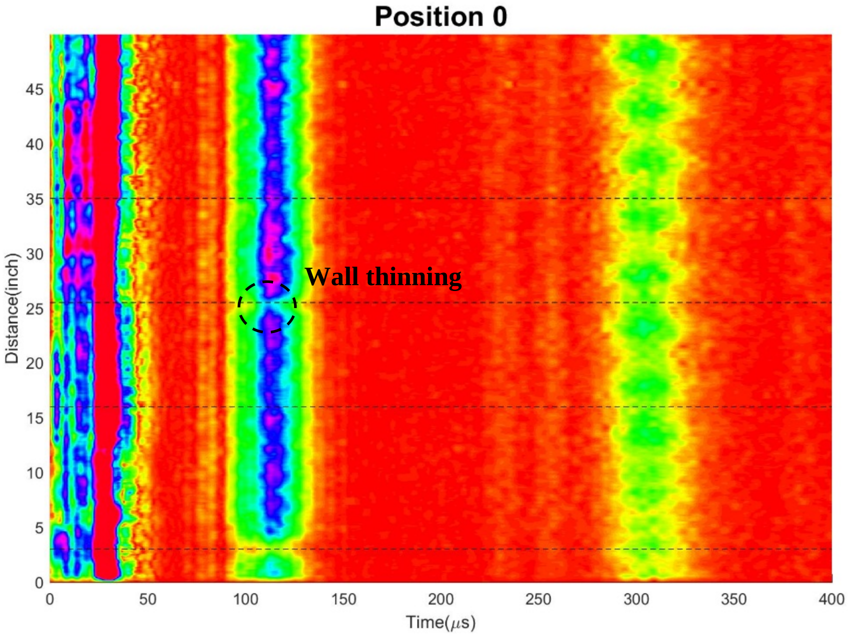

Figure 40. B-scan signals collected at position 0 on the 12-inch pipe

6.5 Discussion on influencing factors

6.5.1 Influencing factors for longitudinal notches and wall thinning

Three influencing factors (i) blind zone due to reflection wave overlapping with transmission wave, (ii) propagation distance, and (iii) inner surface unevenness have been identified to be affecting the detection of longitudinal notches and wall thinning. This section will explain how they affect the detection and the reason behind it.

6.5.1.1 Blind zone due to reflection overlapping with transmission

There are situations where the wave arrives at the Rx at the same time as one of the transmitted wave packets, and the signal cannot be distinguished easily because its amplitude is small compared with the transmission wave packets. Such situations can be found for clock positions 3, 9, 15 and 21 if the separation angle of Tx and Rx is 90°.

However, a more general rule is drawn for an arbitrary angle of separation as shown in if the position of a notch is diametrically opposite to either Tx or Rx, the time-of-flight (TOF) of the reflected signal will be the same as that of a transmitted signal and the signal overlapping happens. Figure 41 (a) and (b) show the conditions when a notch is facing the Tx and Rx respectively. Assume the separation angle between the Tx and Rx is θ, the traveling angle for both transmission and reflection path is $360° - \theta$. This will also result in the same TOF of reflection and transmission signals.

Another case where this is observed is when the notch is at the same clock position as the Tx as shown in Figure 41 (c). The Tx sends both clockwise and counterclockwise waves. After 360° of propagation, both waves arrive the Tx at the simultaneously. Each of them is partially reflected due to the notch at the Tx. The reflection due to the clockwise wave will travel counterclockwise, and the reflection due to the counterclockwise wave will travel clockwise. Thus, both reflection waves will overlay with the transmission wave. If the notch is at the same clock position as the Rx, Figure 41(d), the reflection and transmission signal will also overlap with each other. When a clockwise wave passes the Rx, it also produces a counterclockwise reflection wave. The reflection wave and transmission wave will meet at the Rx again after 360° propagation.

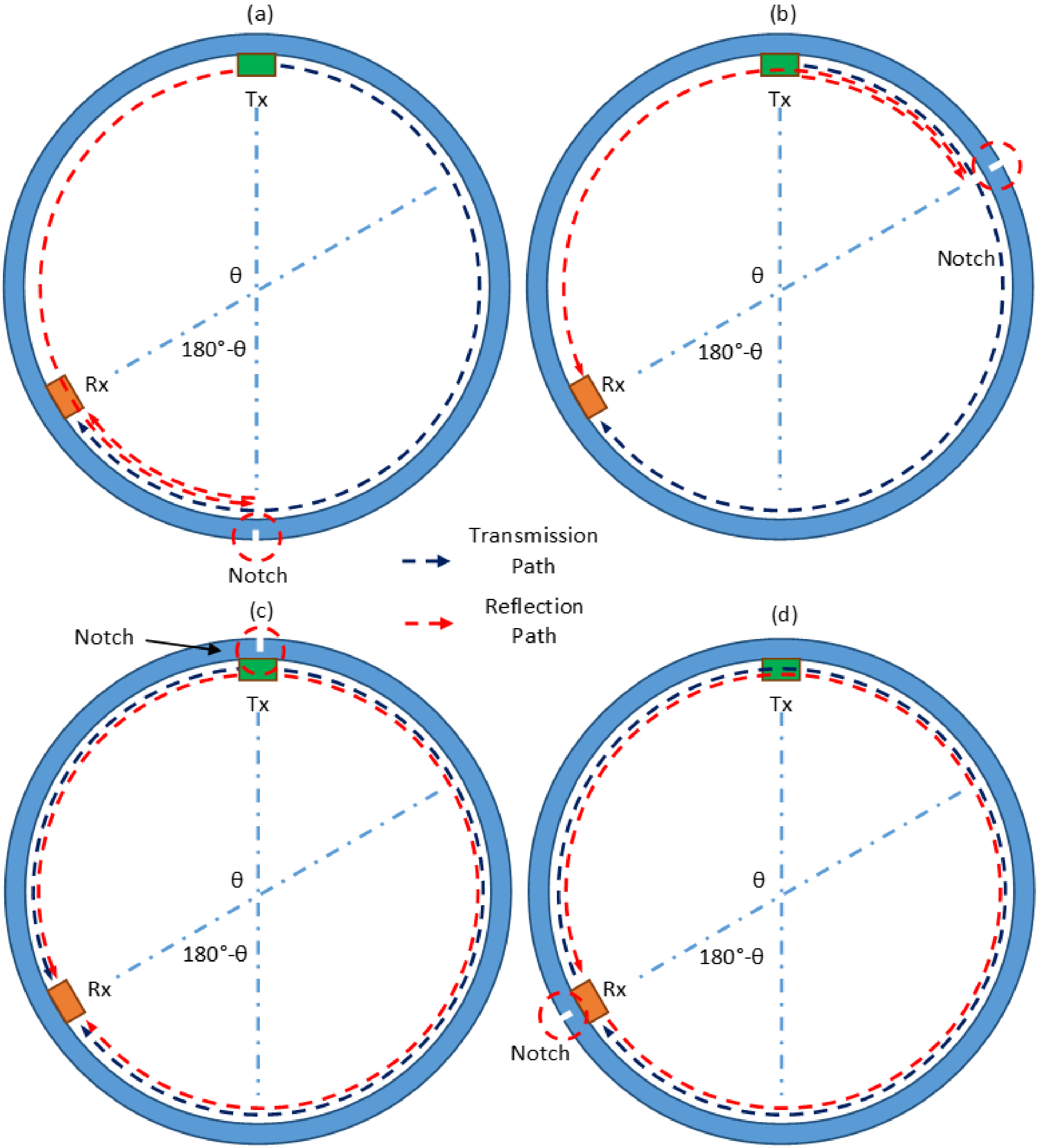

Figure 41. The four conditions when the reflection signal has the same time of arrival as the transmission signal. (a) notch facing Tx, (b) notch facing Rx, (c) notch under Tx and (d) notch under Rx.

As a summary, for any separation angle between the Tx and Rx, there are four special situations where the reflected signal has the same TOF as the transmitted signal. As mentioned in Sec. 3.4, the noise band is wider when a transmitted wave packet is received. The signal overlapping significantly compromises the sensitivity to the defect because the defect-induced signal change may not exceed the noise band. Thus, these clock positions are regarded as “blind zones” for the detection of defects. To determine the four blind zones, two diametrical lines can be drawn to pass through the Tx and Rx respectively. The 4 locations where the lines intersect the circumference are the blind zones. The wave packet has a certain length in time axis because it contains multiple cycles. It is thus anticipated that the overlapping could still happen even when the defect is a few degrees offset from the diametrical lines. This angle should be no more than 15 degrees according to current results because the nearby position, e.g., position 4 and 20, shows good sensitivity. These blind zones can be covered by a second axial line scan if the Tx and Rx together are rotated circumferentially to another position with no overlapping blind zones.

6.5.1.2 Propagation distance

When positioning the Tx and Rx in accordance with Figure 41(a)-(c), it is observed that the amplitude of the reflected signal decreases from (a) to (c). This is because the reflection signal needs to travel a longer distance to be received by the Rx. The longer distance attenuates the reflected signal more.

Ultrasonic guided waves have the diffraction characteristic that is the same as any other type of wave. Due to the diffraction, the amplitude field passing the wall thinning region will reconstruct and restore its amplitude after a certain distance of propagation. This mechanism can be explained using FEA simulation conducted in COMSOL. In Figure 42, the excitation on a steel plate having the same thickness as the pipe wall has been modeled through the multi-physics FEA modeling. A wall thinning defect is also put in the center of the plate and has the same size as that in the experiment. In Figure 42(a), the wave just passed the wall thinning, and it is seen that the wavefield right behind the wall thinning is significantly attenuated. In this situation, it is easier to detect the wall thinning. However, after a certain distance of propagation, as shown in Figure 42(b), the wave field amplitude is restored. The wave amplitude reduction is not that significant and could cause difficulty in detecting the wall thinning. In summary, the distance between the Rx and the wall thinning will influence the sensitivity to the defect.

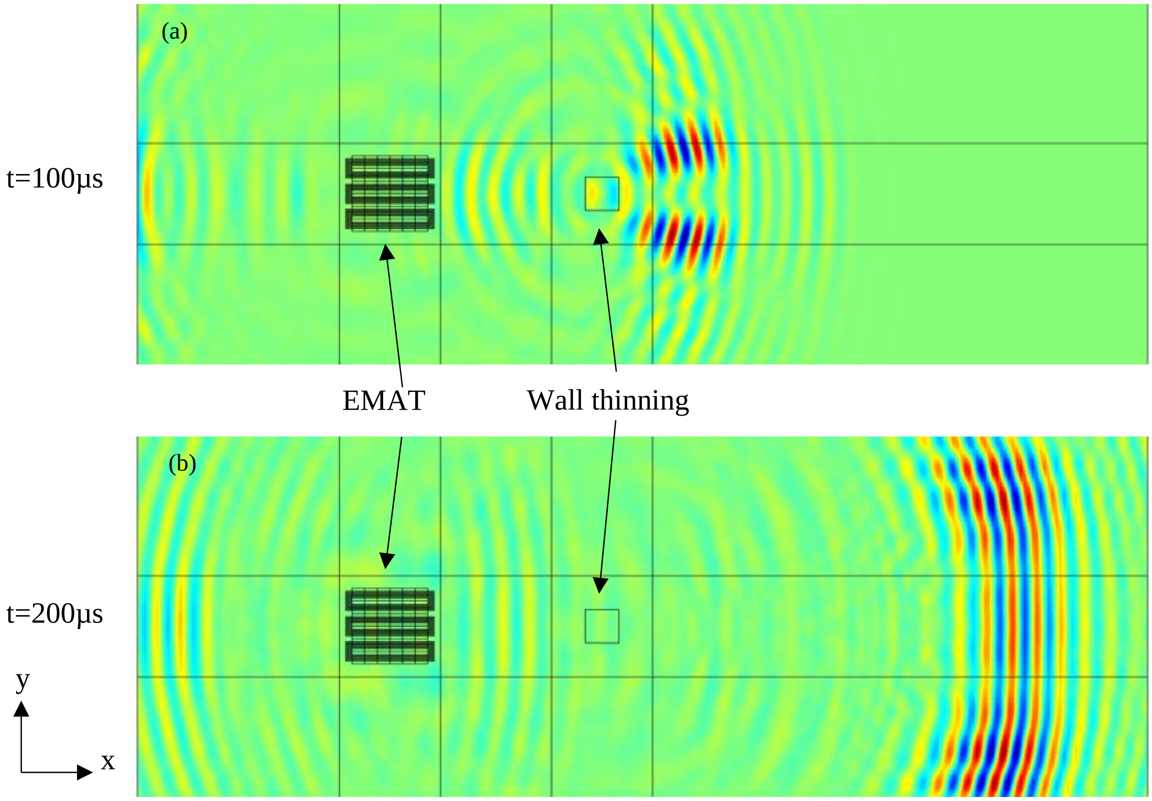

Figure 42. The FEA simulated wave field excited on a flat plate with the presence of a wall thinning.

6.5.1.3 Inner surface unevenness

As shown in Figure 43, periodic ring patterns distributed longitudinally are observed which produce uneven inner surfaces. This induces great variation in the wave amplitude. Such a variation makes the baseline signal very unstable and results in a very wide noise band. The noise band is so broad that all the signals fall into that range and cannot be differentiated from the baseline signals.

Figure 43. A photo of the inner surface of the 12-in steel pipes depicting an uneven inner surface.

6.5.2 Summary of influencing factors

In this section, multiple factors have been investigated and their effects on the sensitivity to longitudinal notch and wall thinning. The following are the findings of the investigation:

(1). There are inherent four blind zones for defect detection given any separation angle between Tx and Rx.

(2). If the distance of the reflection path is long, the sensitivity to the defect is compromised.

(3). The sensitivity is reduced if the defect is on the long path.

(4). The inner surface unevenness produces a very wide noise band when the EMAT is located at these uneven rings, and so defect signals arriving after the 1st signal cannot be distinguished from the noise

Through careful design and arrangement of the EMATs as well as through operational procedures, these limitations can be overcome.

6.6 Algorithm for automated defect identification

In section 3.5, the signature of wall thinning and longitudinal notch was determined. The A-scan signal at defect locations has been compared with the averaged A-scan signal. The averaged A-scan signal has a noise band (±2σ). If an A-scan signal falls out of this band, there is a high possibility that there are defects at this axial location. We have examined the A-scan for defect locations and verified that they are "outliers" with respect to the noise band. However, we have not examined all axial locations, and it is possible that some A-scan signals still fall out of the band even though there is no defect corresponding to it. Generally speaking, it is because of the high-noise nature of EMAT ultrasound. The detailed reason has been discussed in Sec. 3.6. Thus, it is important to examine every A-scan signal and evaluate the situation of false positive, i.e., false alarm.

A defect index has to be developed to evaluate how much an A-scan signal deviates from the averaged signal and noise band. Since the defect signature is different for longitudinal notch and wall thinning, the corresponding defect indices are also different.

6.6.1 Defect index for longitudinal notch: 12" pipe

The comparison of the two defect indexes is shown in Figure 44 with different multiplier values from 2 to 5. Assuming γ is a multiplier in the defect index calculation which sets the threshold, for $Index_1^{Notch}$, through experimentation, it was verified that a high γ is very helpful for defect identification as shown in Figure 44. The next step is to compare the results in different clock positions to study if the defect is located differently with respect to the sensors.

The clock positions 4,5,6,7,17,18,19 and 20 are the 8 cases with shorter propagation distance. The $Index_1^{Notch}$ with γ=3 for these clock positions are plotted in Figure 45. It is observed that in all the cases, the longitudinal notch has been successfully identified by is maximum index value and located accurately for its axial location. The hole is also identified in some cases, i.e. (b), (c), (f) and (h). The varying detectability of the hole is also due to the propagation distance change of the reflected signal. By increasing γ value to γ=5 as shown in Figure 46,, the false positive are again reduced significantly for all the clock positions. This verifies the conclusion that high γ is very helpful for defect identification using $Index_1^{Notch}$.

Similarly, the results for eight clock positions are also plotted for $Index_2^{Notch}$ in Figure 47 and Figure 48 for $\gamma = 3$ and $\gamma = 5$. The improvement of using higher γ value is not as significant. Also, it should be noted that in Figure 48(e), the index value is very low. If we further increase the γ value, the defect can be missed (false negative). Thus it is not beneficial to use $Index_2^{Notch}$ with high γ value. By comparing Figure 46 and Figure 47, they are of the same quality which means similar level of false positive. A tentative conclusion is that $Index_1^{Notch}$ with high γ value and $Index_2^{Notch}$ with low γ value give the best balance in identification of the longitudinal crack in 12-in pipe.

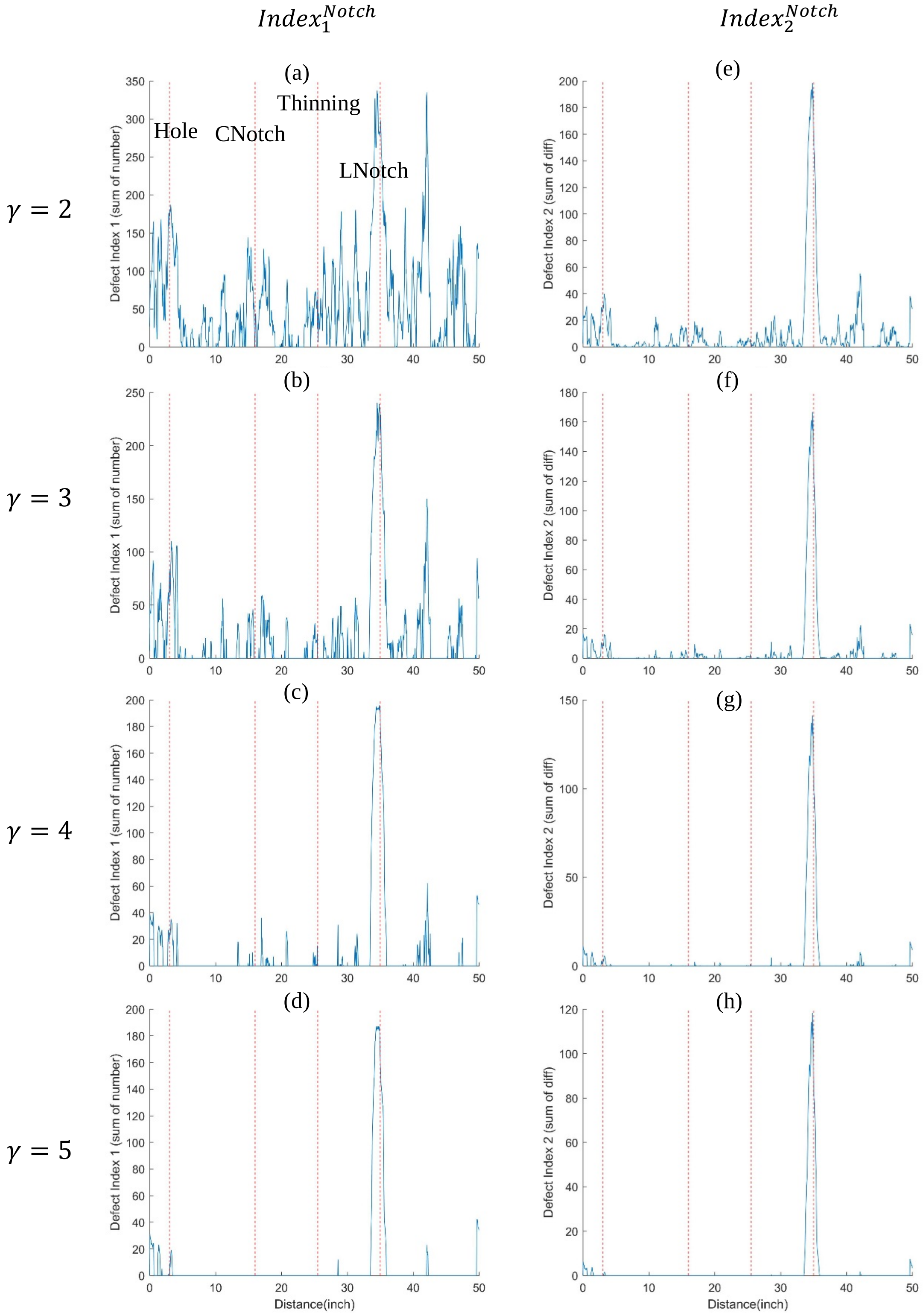

Figure 44. The plot of two defect indexes as a function of scanning distance with different γ values.

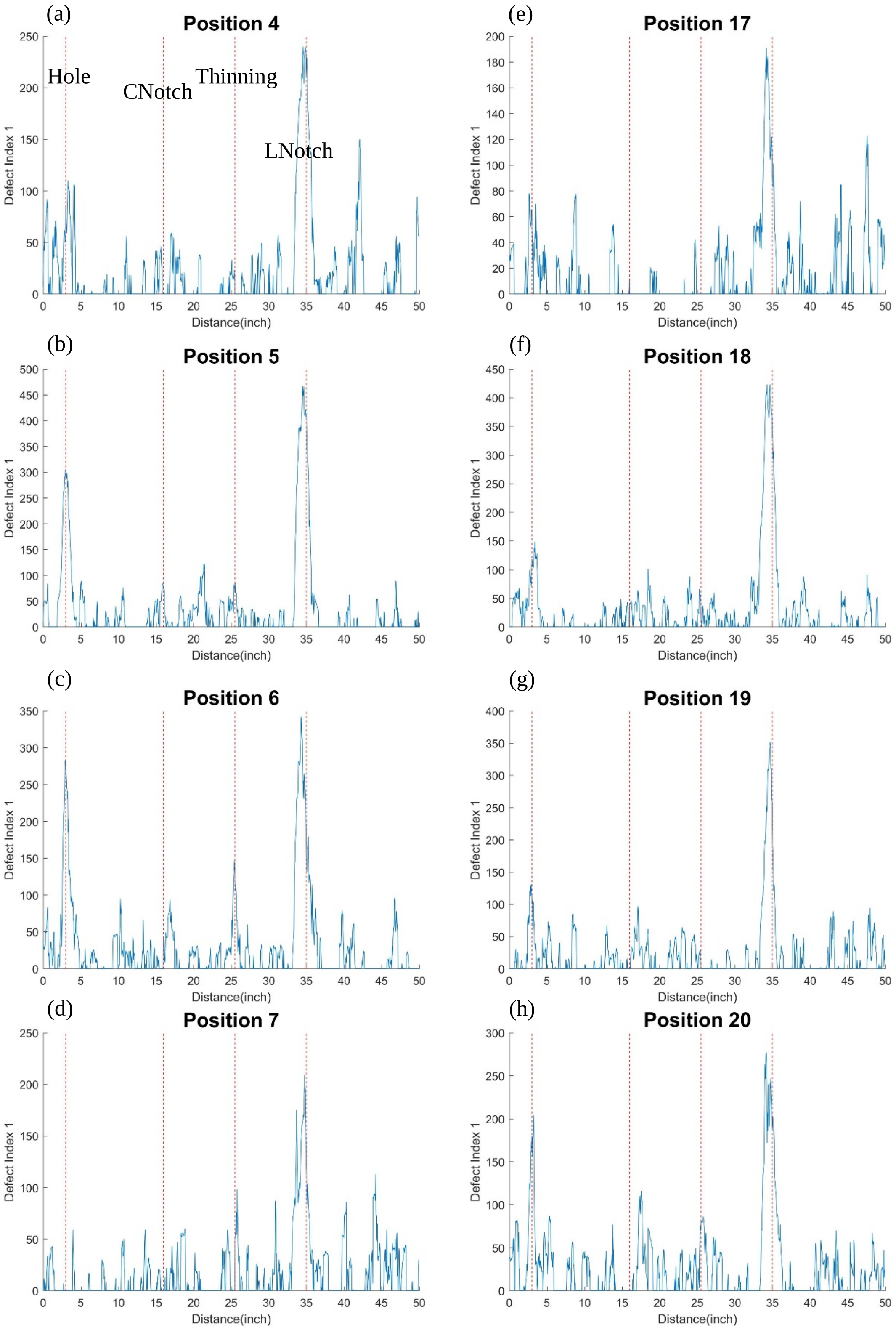

Figure 45. The $Index_1^{Notch}$ for the 4 to 7 and 17 to 20 clock positions with $\gamma = 3$.

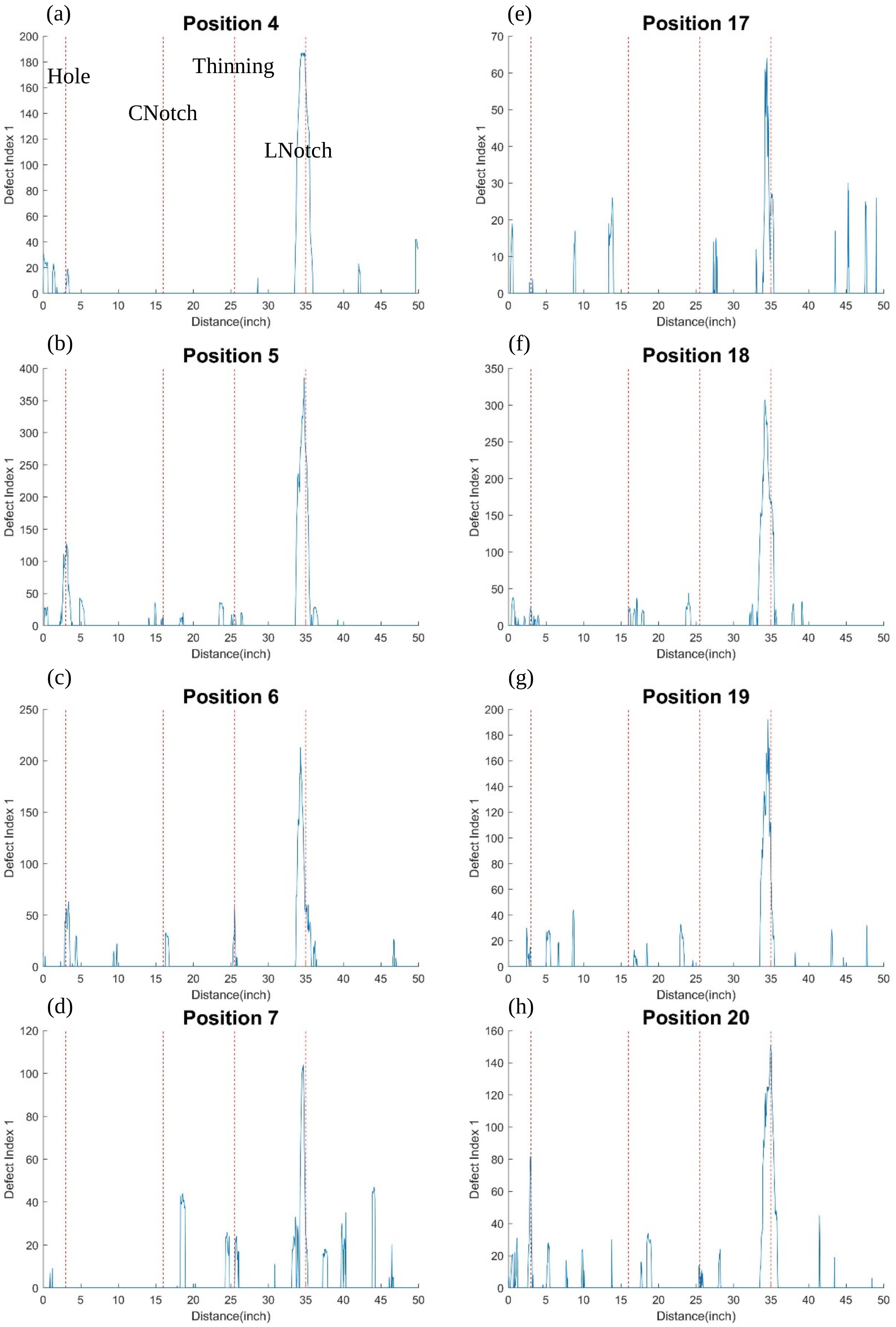

Figure 46. The $Index_1^{Notch}$ for the 4 to 7 and 17 to 20 clock positions with $\gamma = 5$.

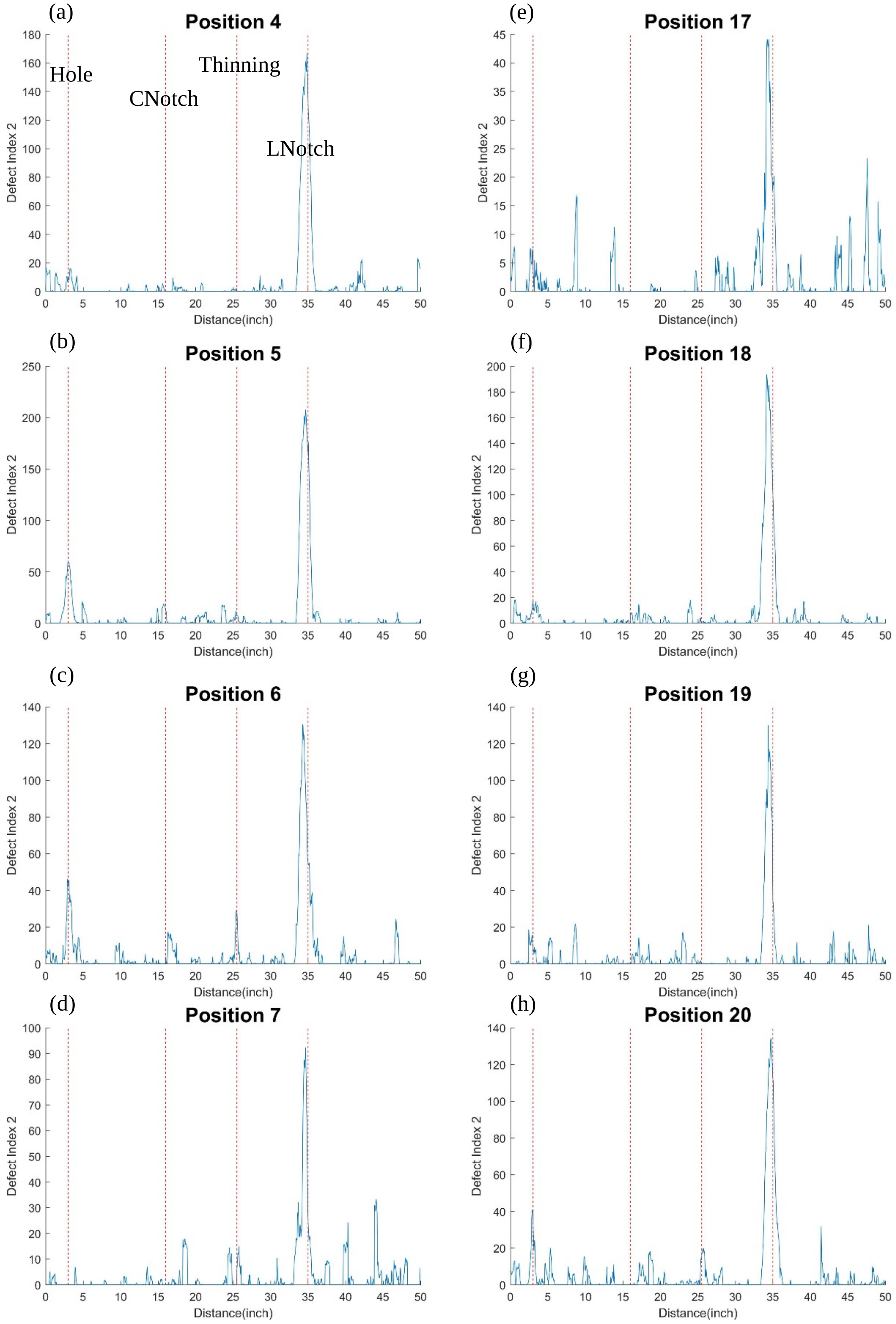

Figure 47. The $Index_2^{Notch}$ for the 4 to 7 and 17 to 20 clock positions with $\gamma = 3$.

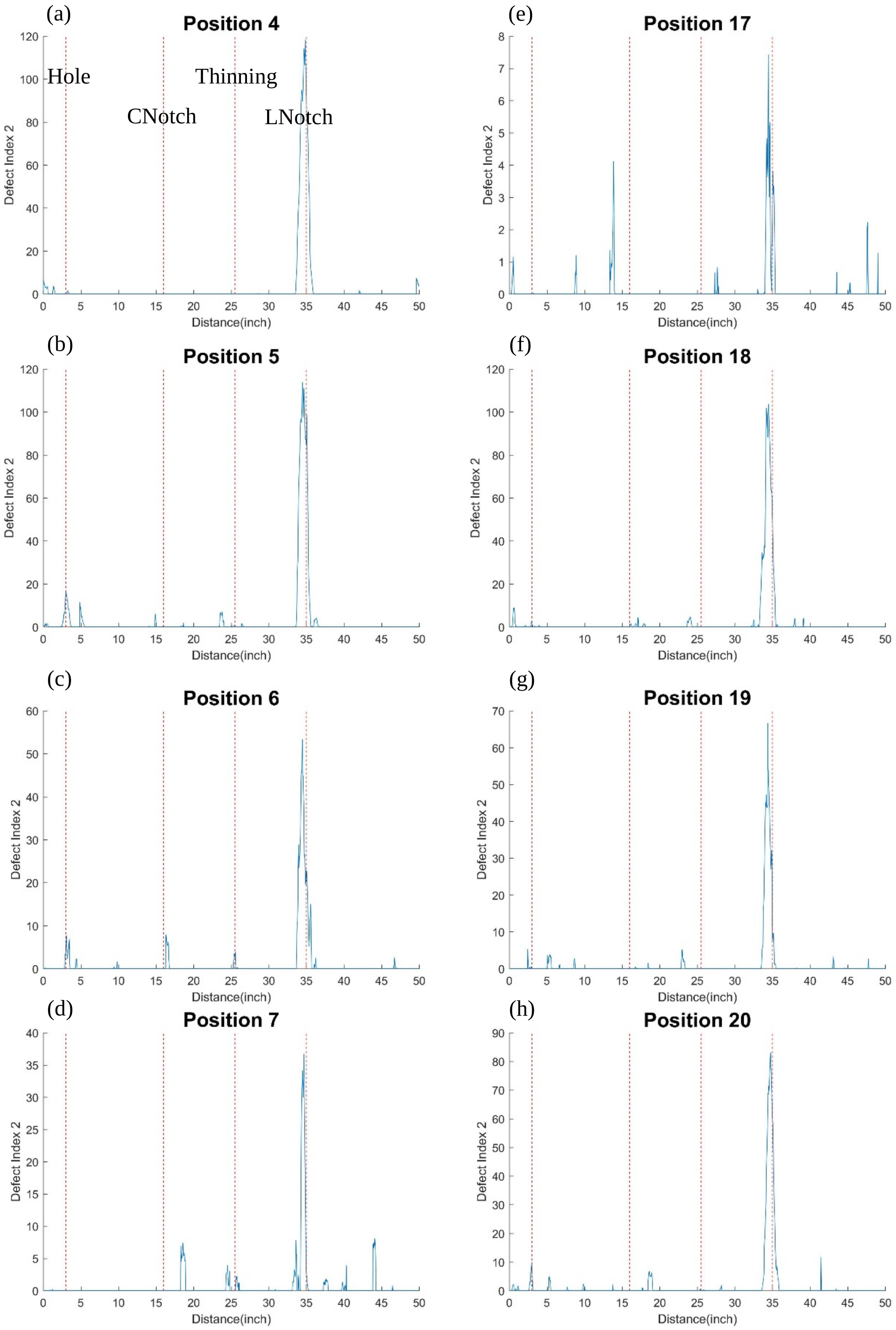

Figure 48. The $Index_2^{Notch}$ for the 4 to 7 and 17 to 20 clock positions with $\gamma = 5$.

6.6.2 Defect index for longitudinal notch: 24” pipe

Applying the same method of calculation of defect index to 24-inch pipe, it was found that the notch detection is successful in certain clock positions but with a high rate of false positives. This is the result of the high noise level in the 24-inch pipe because of longer propagation distance and the uneven surface of the pipe wall. Also, the detection of the longitudinal notch fails at certain positions.

By using additional post-processing methods, the noise can be mitigated, these post-processing methods significantly improve the detectability, and the enhanced results are shown in Figure 49 and Figure 50.

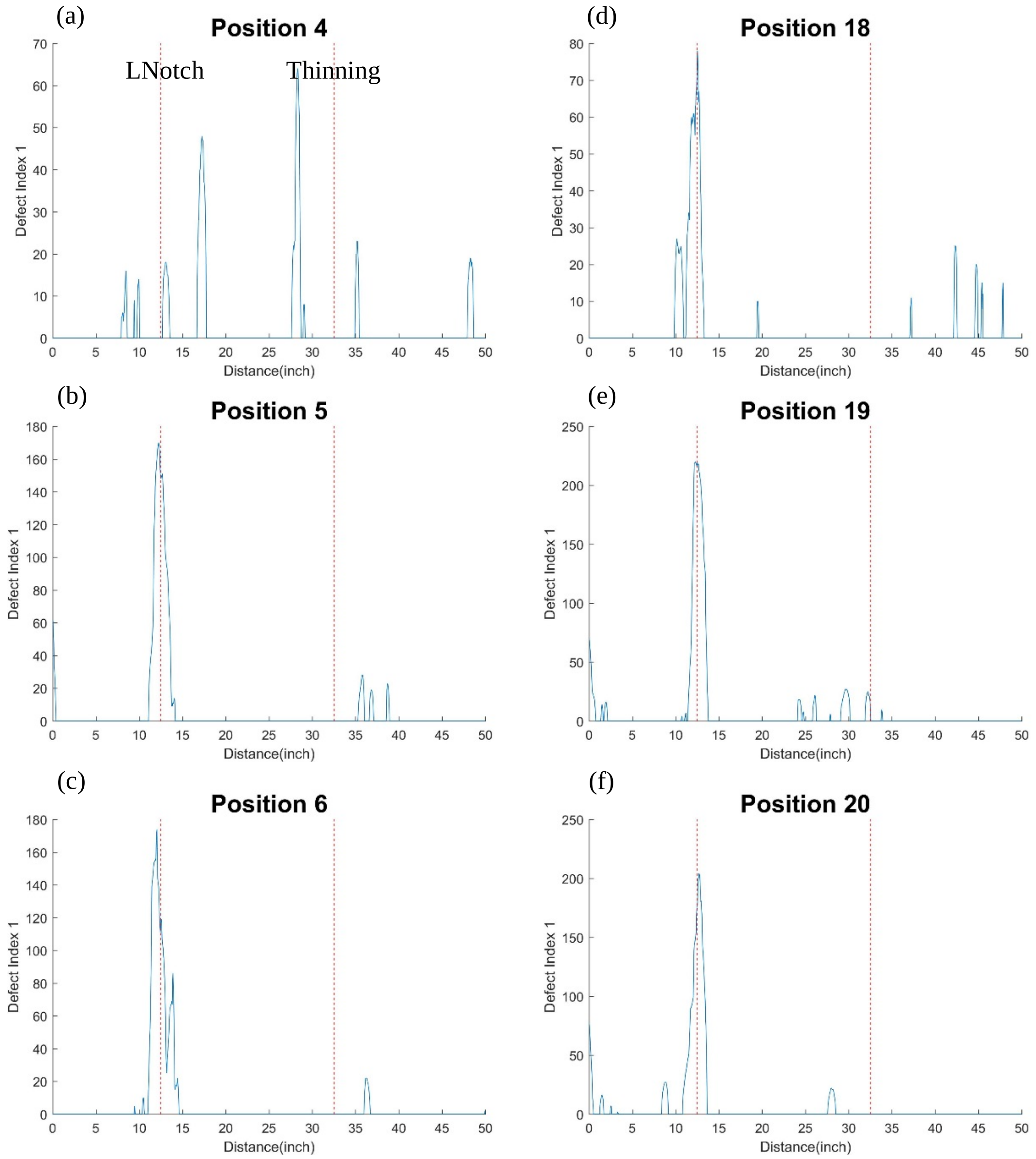

Figure 49. The $Index_1^{Notch}$ for the 4 to 6 and 18 to 20 clock positions in 24-in steel pipe with $\gamma = 3$, enhanced by post-processing methods.

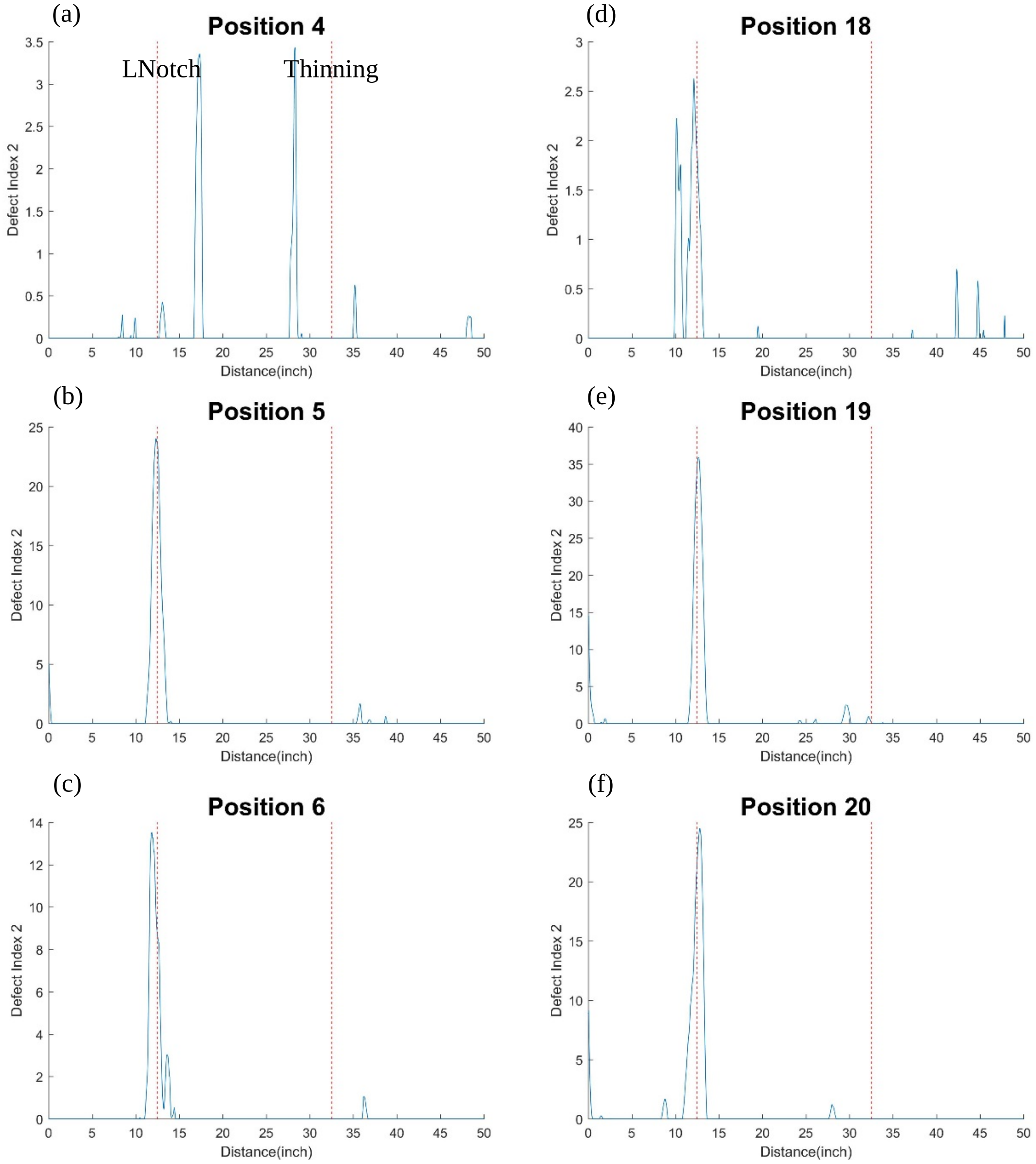

Figure 50. The $Index_2^{Notch}$ for the 4 to 6 and 18 to 20 clock positions in 24-in steel pipe with $\gamma = 3$, enhanced by post-processing methods.

6.6.3 Defect index for wall thinning: 12” pipe

For the 12-inch pipe, the clock positions 0, 1, 2, 22 and 23 correspond to the best detectability. Using large γ values like 3 or 5 in the wall thinning detection will make the threshold too strict. As shown in Figure 51(b)&(d), this will have the risk of missing the detection, i.e., false negative. Thus, $\gamma = 2$ is selected as a reasonable threshold and used in the following analysis.

In Figure 52 and Figure 53, $Index_1^{Thinning}$ and $Index_2^{Thinning}$ as functions of the axial location are plotted for five clock positions when the defect is on the short path. The through hole gives the greatest index value in all cases. This is not a surprise because the through hole removes lots of material and is undoubtedly the most severe damage on this 12-inch pipe. The wall thinning always gives the second highest index value which means the wall thinning can be easily detected as an “outlier” if no through-hole is present. The results of using $Index_2^{Thinning}$ are much better than using $Index_1^{Thinning}$ because there are fewer false positives.

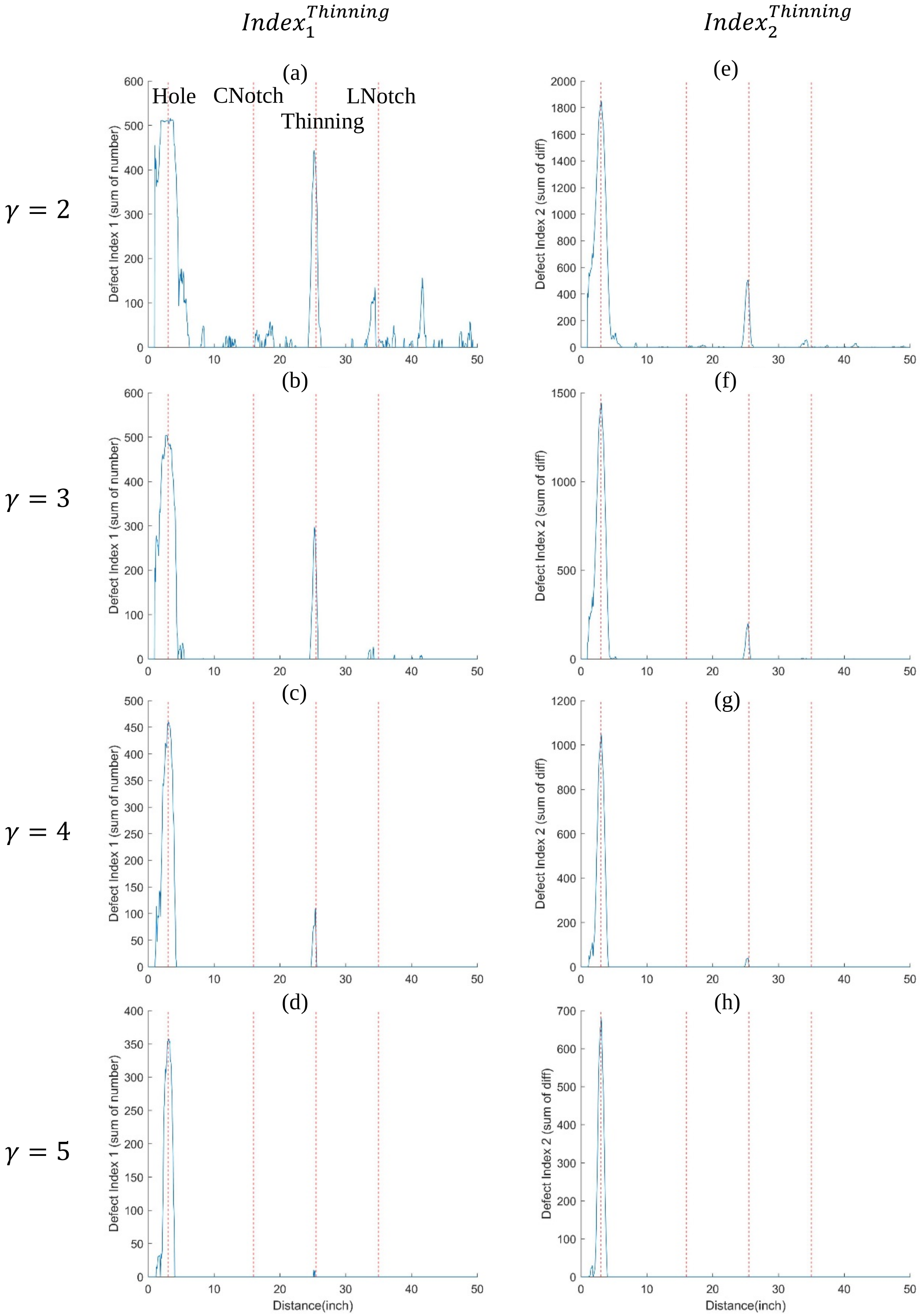

Figure 51. The plot of two defect indexes as a function of scanning distance with different γ values. The signal is collected at position 0 on the 12-inch pipe.

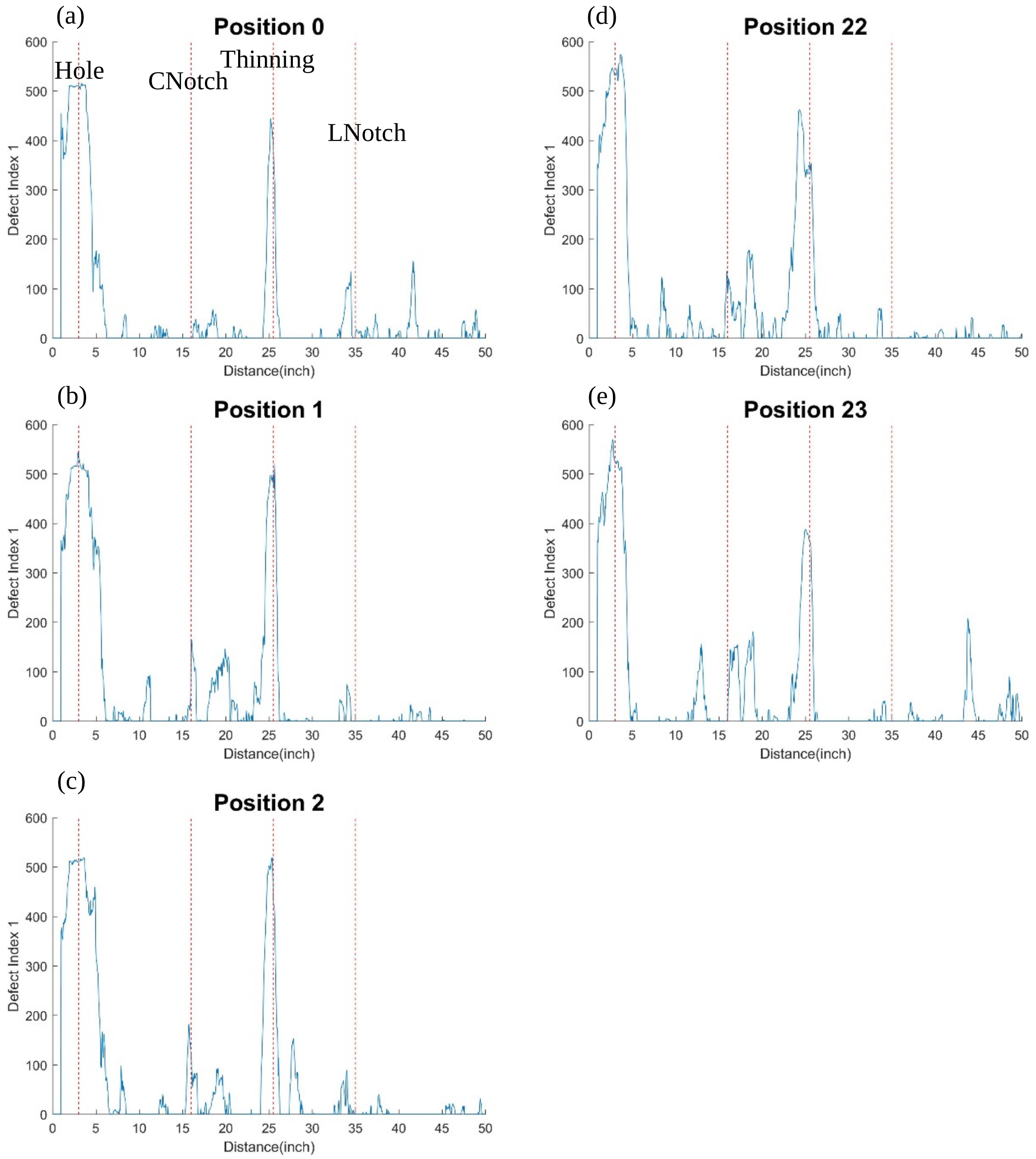

Figure 52. The $Index_1^{Thinning}$ for clock positions 0, 1, 2, 22 and 23 in 12-in steel pipe with $\gamma = 2$.

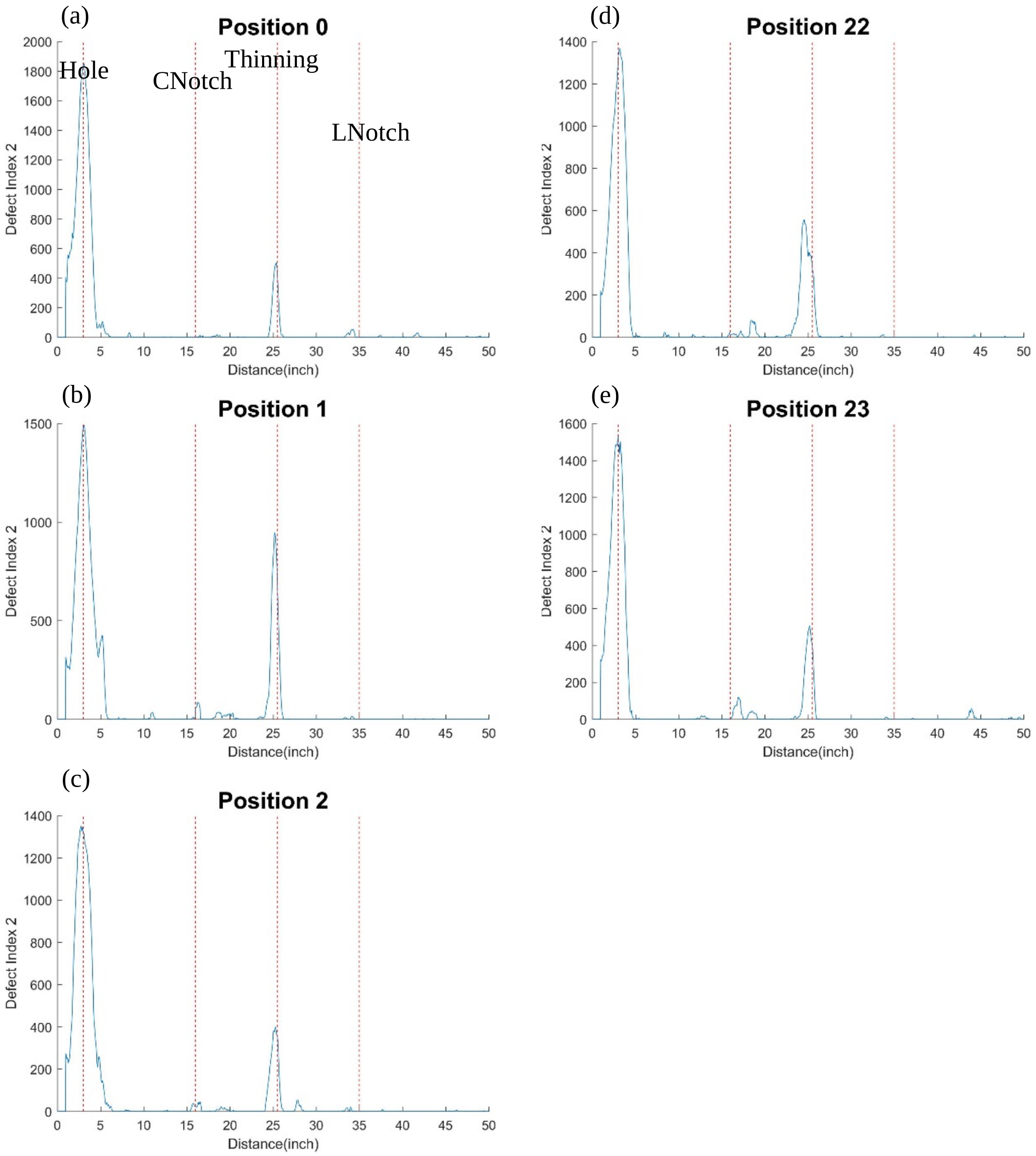

Figure 53. The $Index_2^{Thinning}$ for clock positions 0, 1, 2, 22 and 23 in 12-in steel pipe with $\gamma = 2$.

6.6.4 Defect index for wall thinning: 24" pipe

The same algorithm is applied to the 24-inch pipe. The results are shown in Figure 54 and Figure 55. Using $Index_2^{Thinning}$ with $\gamma = 2$ gives the better detectability and less false positives.

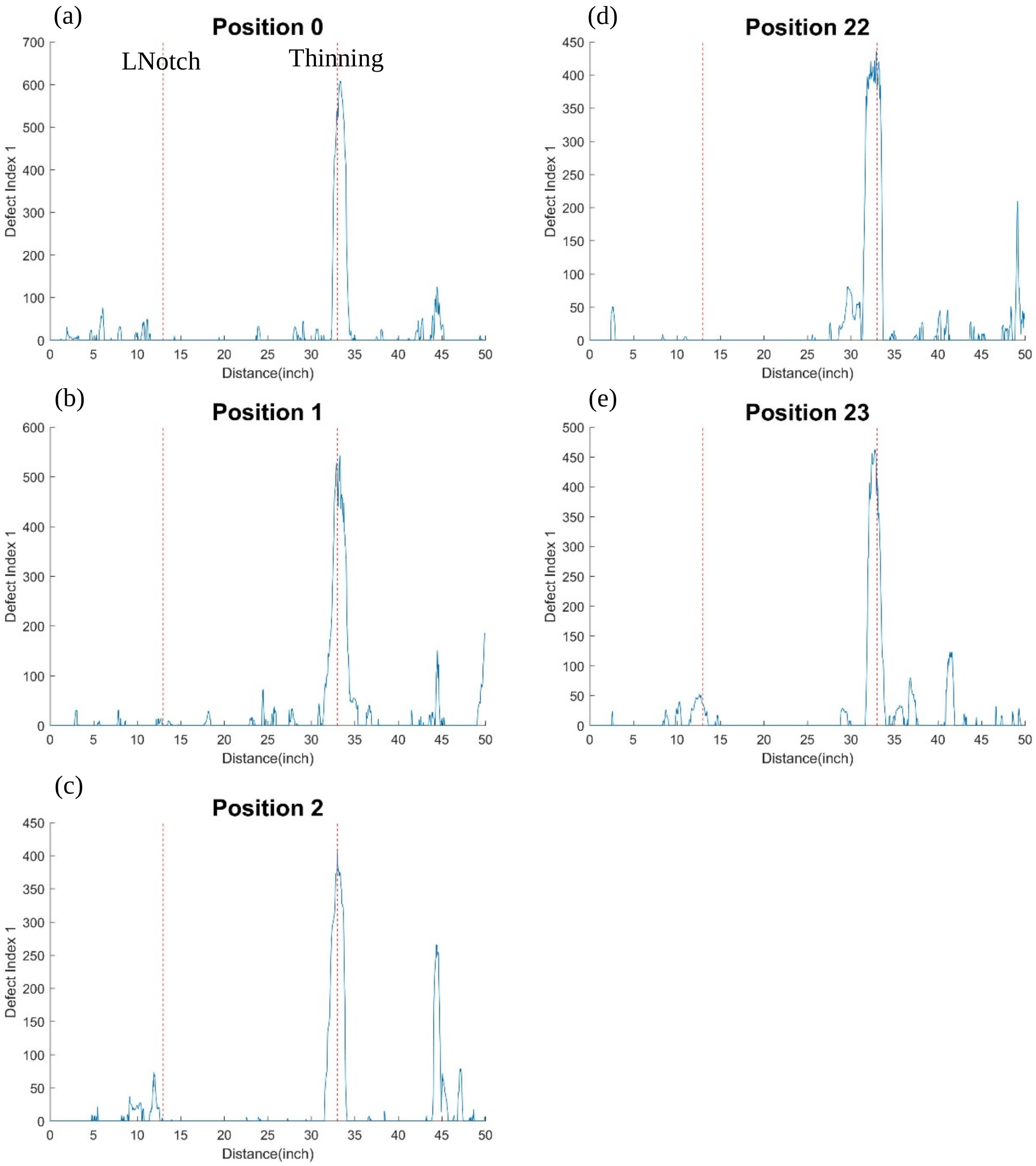

Figure 54. The $Index_1^{Thinning}$ for clock positions 0, 1, 2, 22 and 23 in 24-in steel pipe with $\gamma = 2$.

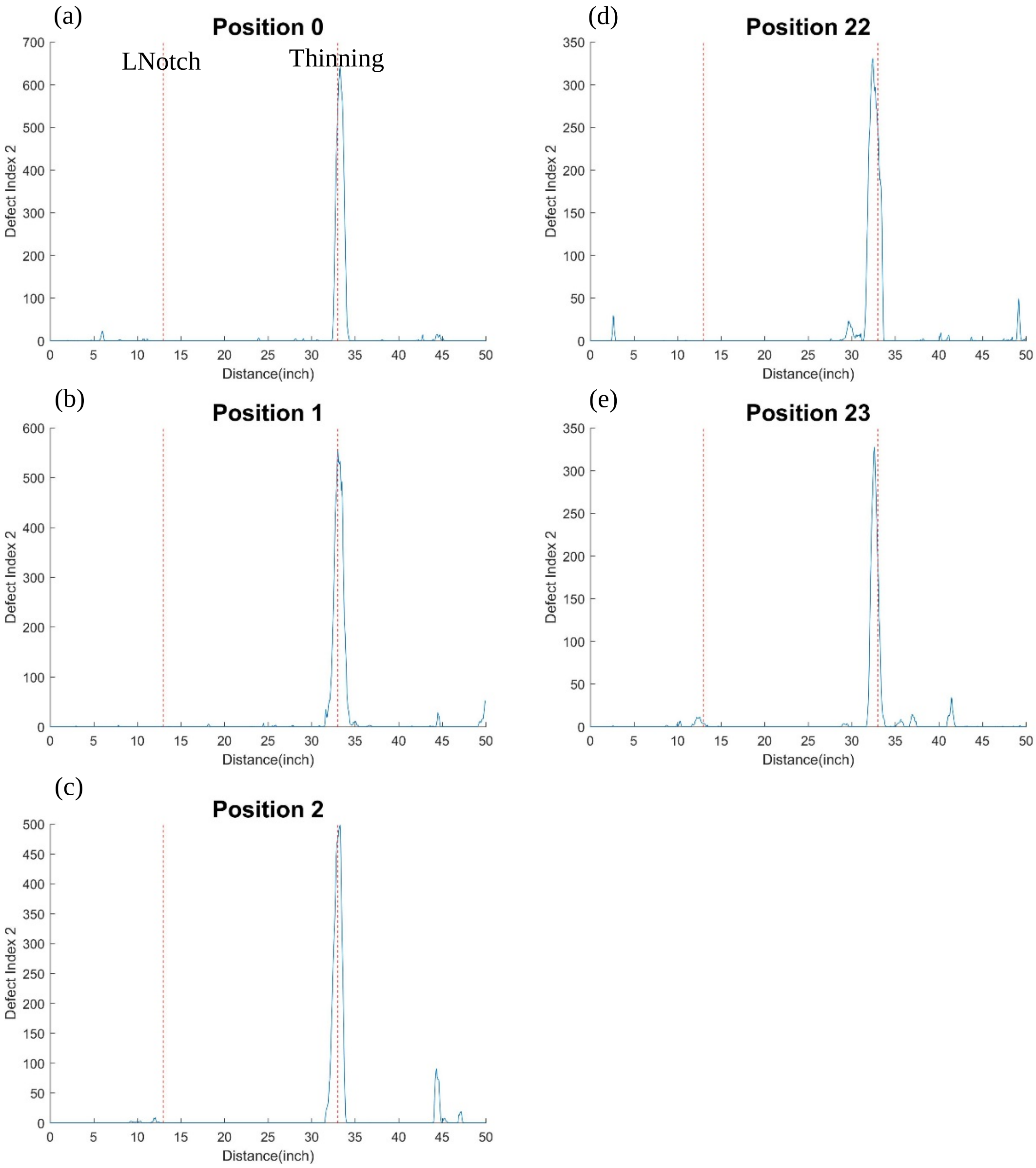

Figure 55. The $Index_2^{Thinning}$ for clock positions 0, 1, 2, 22 and 23 in 24-in steel pipe with $\gamma = 2$.

6.7 Pipe Test Summary

The pipe test has produced lots of results and provided a number of meaningful findings. Some important conclusions are highlighted below.

1. The pipe test covers a good range of pipe geometry, material, and type as well as defect type and size. The results are representative enough to guide any further research and design work.
2. The A-scan and B-scan plots provide useful and easy-to-understand ways to review the inspection results.
3. A rigorous (4-sigma) noise band has been overlaid on the baseline signal for defect detection to minimize the effect of surface unevenness and false positive rate.
4. The longitudinal crack-like defects can be effectively detected, located and characterized.
5. The local metal loss can be detected, axially located. To locate the defect circumferentially, it is possible to use more EMATs to improve the locating resolution. To characterize defect size, more calibration work is needed in the future.
6. Guided waves have been found to be sensitive to both crack-like defect and local metal loss.
7. There are intrinsic blind zones corresponding to the detection technique, and they are unavoidable. It can be overcome by optimizing the arrangement of the EMATs or developing an operational plan for scanning to cover all blind zones.
8. The sensitivity to crack-like defect and local wall thinning is also distance-dependent.
9. Changing the separation angle of Tx and Rx could improve the sensitivity to defects.
10. The surface condition has a great influence on the quality of baseline signals; the ERW pipe has a better surface geometry than the seamless pipe.
11. Defect index has been developed for easy representation of the inspection results for operator use without knowing the nominal pipe signal.

7 SPECIAL CASES

7.1 Soil test

7.1.1 Introduction

The objective of the soil test was to study the effect of soil covering the pipe on the wave propagation. In the literature, it has been found that for guided waves propagating along the axial direction of the pipe, the soil could attenuate the wave [1]. However, the circumferential waves used by ULC only travel short distance compared with the longitudinal guided wave used in the literature. The effect of the soil on the wave attenuation was hence reevaluated.

7.1.2 Experiment Setup

7.1.2.1 Selection of Soil

The sand was selected for the primary experiment because it was found that for current steel pipe, the backfill materials were usually rock-free sand. However, to not lose generality, common garden soil was also taken into consideration to make a comparison. The buried pipe test box had three compartments, and only two were filled with sand and garden soil respectively. The sand was Sakrete multi-purpose sand, and the soil was Miracle-Gro garden soil.

7.1.2.2 Buried Pipe Box

Figure 56. Buried Pipe Test Box for the soil test of the 12-in steel pipe.

Figure 57. 12-in pipe in the empty buried pipe test box.

The test box is shown in Figure 56 without the pipe installed. Figure 57 shows the 12-in pipe and the test box used for the soil test. The dimensions of the box are listed in Table 8

Table 8. Dimensions of the whole test stand and its two compartments for sand and soil.

	Length (in)	Width (in)	Depth (in)
Whole	53	22.5	24
Compartment 1 (soil)	16.5	22.5	24
Compartment 2 (sand)	20	22.5	24

Figure 58. The sand compartment before filling with sand and the pressure sensor is bonded at the bottom with double-sided tape.

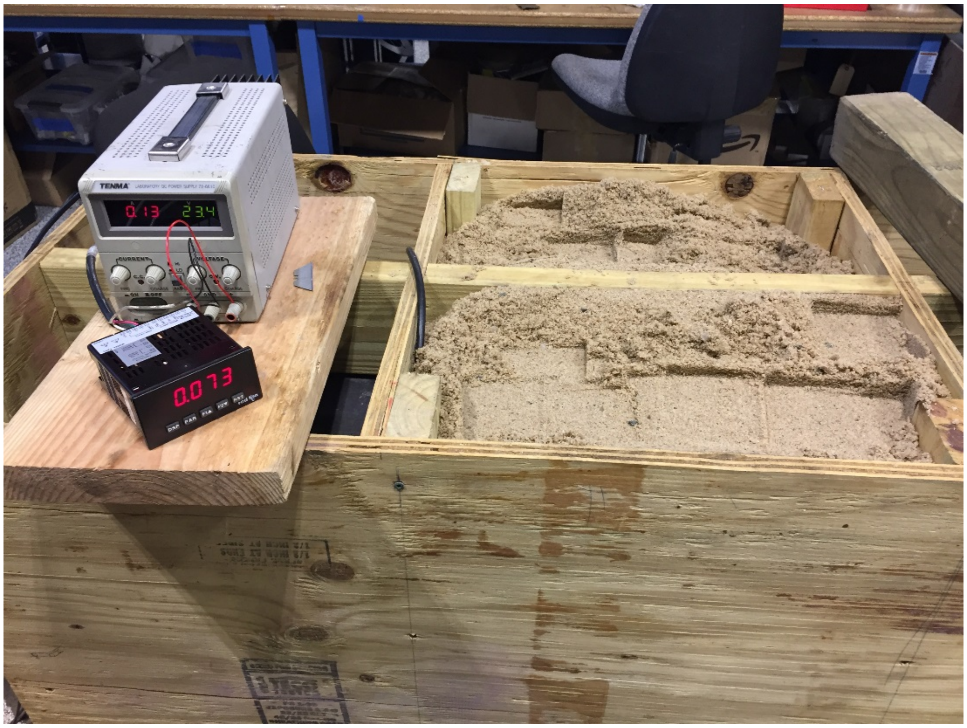

Figure 59. The sand compartment right after filling the sand and the sand is compacted with a wooden post manually.

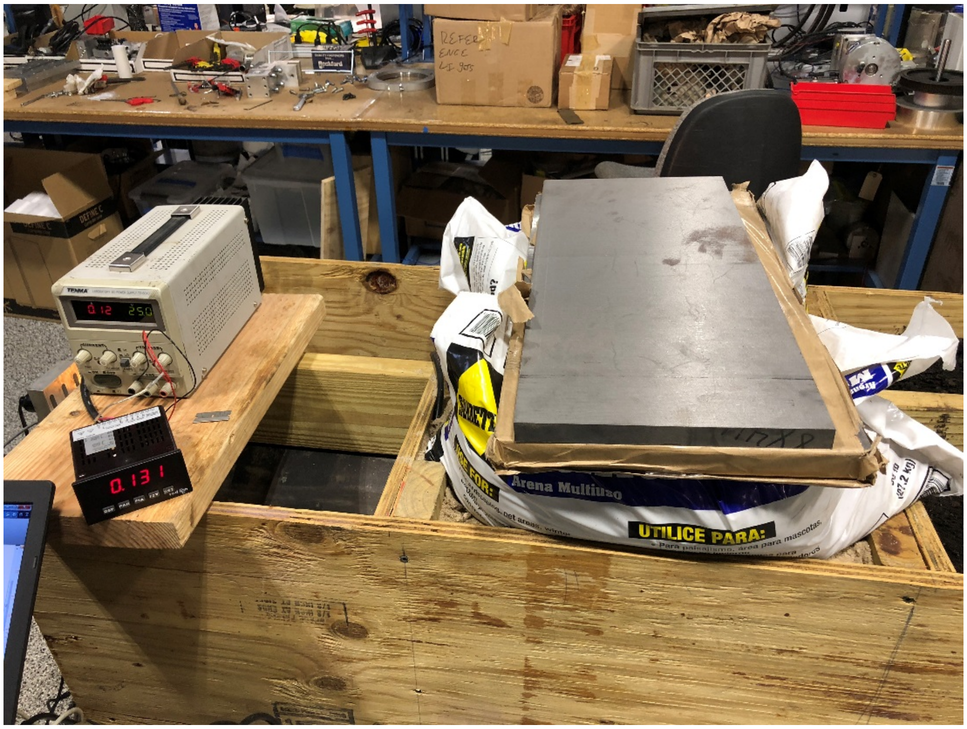

Figure 60. The sand compartment with applied deadweight on the top.

For the compartment with sand, a soil pressure sensor was put at the bottom of the wood box (Figure 58). The soil sensor was KDC-200KPA which had the maximum measurable pressure of 200 kPa. There were two conditions applied to the sand compartment, (1) right after the sand is added to the compartment and the sand is compacted manually, as shown in Figure 59, and (2) three days after putting deadweights on the top of the sand as shown in Figure 60. The original plan was to measure the pressure of the newly added sand. However, it was noted that the sand from the bag had a certain level of moisture. The condition (1) had loose sand and the moisture making this the soil pressure not stable since the sand was getting drier and further compacted due to its own weight. Thus condition (1) was only an intermediate condition and not used for the study. For condition (2), some deadweights were applied on the top of the sand, and the whole setup was left there for three days to have the sand further compacted and settle down, Such condition is considered as the buried condition. The pressure measured was 5.3 kPa measured with the pressure sensor for condition (2).

7.1.3 Experiment Procedure and Data Processing

To study the attenuation of the wave propagating in the pipe in the presence of sand and soil, two modes, were chosen for the study because they were non or low dispersive and their wave packets did not spread after a long distance of propagation. The transmitter (Tx) and the receiver (Rx) were separated by 90°. The total scan distance was 50” which is exactly the same as that used in the pipe test report. After each scan, the Tx and Rx were rotated together by 45°. Thus there were eight scans, and the whole pipe circumference was covered. These 8 locations were the position 0, 3, 6, 9, 12,15, 18 and 21 described in the pipe test report (final version). To be consistent, the same naming convention was used in this report.

As mentioned above, the test box had three compartments, and two of them were filled with soil and sand. Thus, there were 3 different sections: soil filling, sand filling and no filling condition. The scanning distance is 50” or 1270 mm which covers all 3 sections. The start and end locations are listed in Table 9.

Table 9. The location of the boundaries between different sections.

Section	Start (mm)	End (mm)
Soil	1	356
Sand	357	889
No-Filling	890	1270

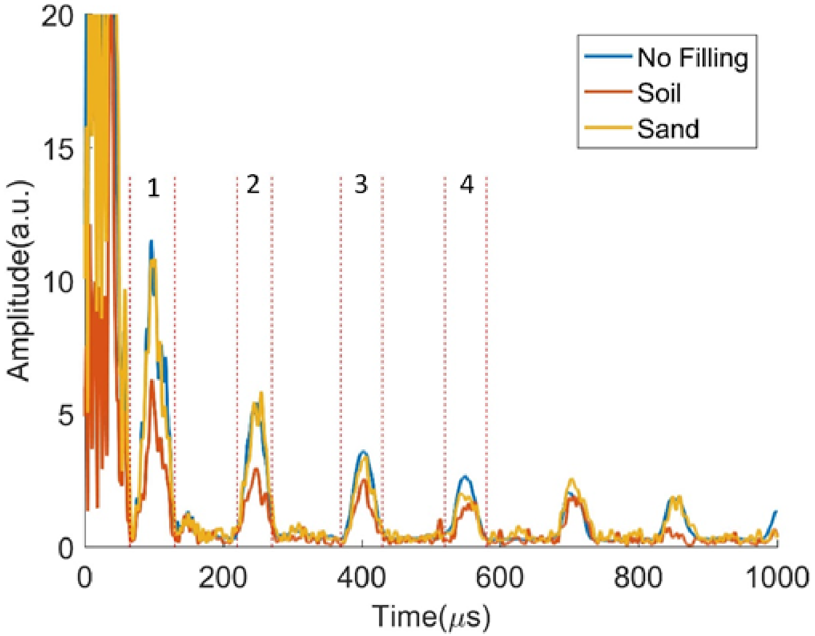

Figure 61. The averaged amplitude envelops for no-filling, soil and sand conditions. The windows for picking the 4 transmission peaks are labeled. The signal is collected at the rotational position 0.

It should be noted that even though there are defects on the pipe, the defects should not affect the results because the defects are the same for both unburied and buried cases and the change is introduced by soil only.

7.1.4 Test Results

7.1.4.1 Attenuation

It was observed that for one mode there is a clear decreasing trend because the peak with longer time of flight corresponds to longer propagation distance and the wave is subject to more significant attenuation due to the soil. For the other mode, a decreasing trend is also clearly observed.

7.1.4.2 Time-of-flight Change

To study the time-of-flight (TOF) change, the envelopes of the A-scan signals before and after filling the soil were compared. It was observed that the rising edges of signals before and after filling the soil are almost overlapping which indicate that they have the same TOF. This is the case for both modes. Similarly, for the signals affected by sand filling, the rising edges still show no shift. So, the sand does not affect the TOF as well.

7.1.5 Conclusion of Soil Test

To summarize the study of the soil effect on the wave propagation, the following conclusions are highlighted:

- Both sand and garden soil could reduce the wave amplitude as it is propagating. This is verified because the wave attenuates faster in the presence of garden soil and sand. The longer the wave travel distance, the more is attenuation on the peak amplitude due to soil impact.
- The time-of-flight is not affected by the garden soil, and sand for both wave modes studied. Theoretically, the pipe without soil and the pipe with soil can be considered as two different waveguides. Their dispersion curves can be different depending on the coupling between the soil and the pipe. However, such difference is so small that it cannot be seen in the experiments. Thus, the time-of-flight is practically the same.
- For real-world practice, the effect of soil and sand is considered not significant because the damage features employed so far by ULC are all existing at short propagation distance, i.e., first one or two peaks. In such short distance, the effect of soil and sand is minor compared with the change induced by the defects. Also, by reducing the separation angle between Tx and Rx, the soil impact can be even reduced. This is a benefit of using circumferential wave for scanning compared with the long-range ultrasonic testing (LRUT). LRUT is well known for its greatly reduced propagation distance in the buried pipe. However, this will not be an issue for the scanning method.

7.2 Debris Test

In a real-life scenario, the pipe wall surface may be covered by debris and corrosion. To get an idea of the performance of EMAT in this condition, ferrite oxide (Fe_2O_3) powder is distributed at the 6:00 position of the 24-inch seamless pipe and the Tx EMAT is traveling on it, as shown in Figure 62. The results compare the wave amplitudes before and after introducing the powder (shown in Figure 63). It is observed that the wave amplitude is decreased a little bit after putting the powder into the pipe. Since the amplitude reduction is minor, it is expected such corrosion powder will not influence the performance.

Figure 62. A photo showing the ferrite oxide powder at the bottom of the pipe.

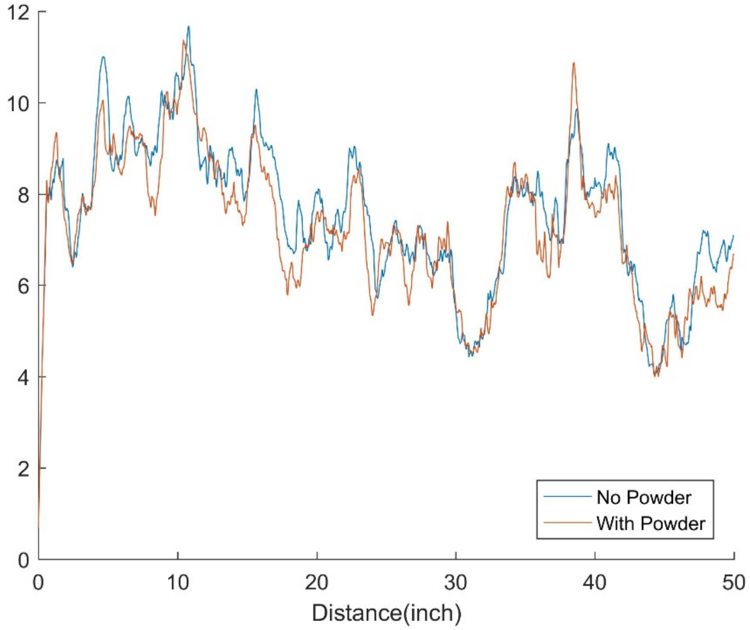

Figure 63. The wave amplitude along the scanning distance for no powder and with powder conditions.

8 COUPLING CONDITION

The coupling condition between EMAT and the pipe is of critical importance to a successful inspection. Even though EMAT is usually claimed to be a non-contact method, it must work within very small proximity of the specimen, usually a few millimeters. For the pipes in service, there could be corrosion and scale build up on the inner surface of the pipe and cause difficulties to maintain a good coupling condition.

There are two factors affecting the overall coupling condition

1. Liftoff. Assuming the sensor surface is parallel to the pipe wall, the liftoff is the distance between the surface of the sensor and the pipe. A small liftoff will make sure both the wave strength and sensitivity are high. A consistent liftoff guarantees that the change in wave amplitude is not due to the poor coupling condition which could introduce lots of “false positive” issues. In real life scenario, the debris, scale and corrosion layer can all cause inevitable liftoff increase.
2. Tilt. The EMAT is also subject to tilt along the circumferential and longitudinal direction due to the unevenness of the pipe surface. When the sensor is tilting, its surface is not parallel to the pipe surface. It is thus expected that one side of the coil is further from the pipe surface than the other side. Since this causes the effective or average liftoff change, such change is also considered as a general liftoff change in the following discussion.

ULC is aware that maintaining the liftoff in pipe inspection is a big challenge and has made efforts on multiple ideas and topics to mitigate the liftoff issue.

9 CONCEPTUAL DESIGN MODIFICATIONS TO CIRRIS XI^{TM} ROBOT FOR GUIDED WAVE EMAT INTEGRATION

The focus of this conceptual design has been on modifying the design of the robot to solely integrate and operate the guided wave EMATs in 24” diameter, cast iron, distribution mains. Here are some highlights about the design and operation:

- The robot will operate in 24” to 30” cast iron pipe.
- One transmitter and one receiver will be separated by 90 degrees along the pipe circumference.
- The center body will be modified to incorporate guided wave EMATs on both sides of the body.
- Under launch conditions, the EMATs are maintained in a stowed position.

Figure 64 shows an isometric view of the CIRRIS XI robot that was previously designed for deploying the wall thickness EMAT sensor. The robot can operate in 24” to 30” cast iron pipe. The design has been updated to incorporate the EMAT guided wave sensors.

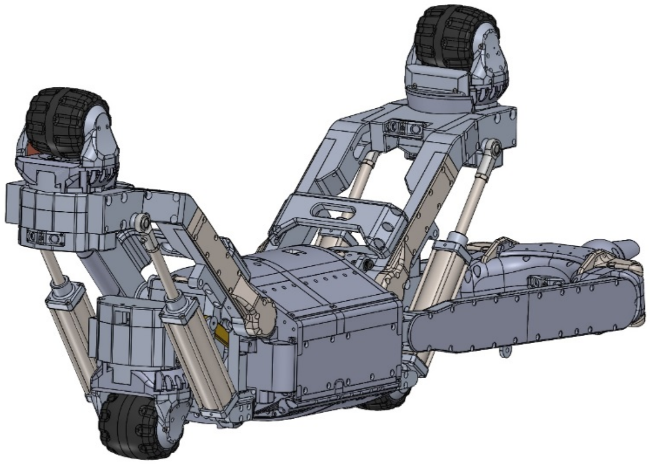

Figure 64. CIRRIS XI^{TM} Design for Deploying Wall Thickness EMAT

The prototype EMATs have also been designed, fabricated and tested for operation in pipe. Figure 65 shows the bottom and top isometric view of the 3D model of the EMAT housing. The EMAT has been designed with the following features:

- Custom curvature to match pipe curvature – The coil and magnets are designed so that they adapt to the curvature of the pipe.
- Robust and lightweight housing – The housing is made of Aluminum and provides sufficient strength to weight ratio to withstand bending forces and other forces that may be imparted to the housing during operation. The housing is able to survive after being scratched or dented by abrasive surfaces in the pipe.
- Reduced friction - Rollers are placed on the sides of the housing to constrain the motion axially along the pipe walls. By incorporating rollers, the amount of drag forces on the robot is reduced allowing for the CIRRIS XI^{TM} robot wheels/drives to be used without modification.
- Reusable Housings – The EMAT housing size corresponds to the largest housing size to incorporate various coils and magnet types to excite different wave modes. Inserts have been developed that can be exchanged into and out of the housing and so the housing can be reused.
- Exchangeable Housings on Robot– The EMAT housings can be exchanged in and out of the robot through removal and installation of a few fasteners. This allows the robot to be fitted with the appropriate EMATs that have a custom curvature for each pipe diameter.

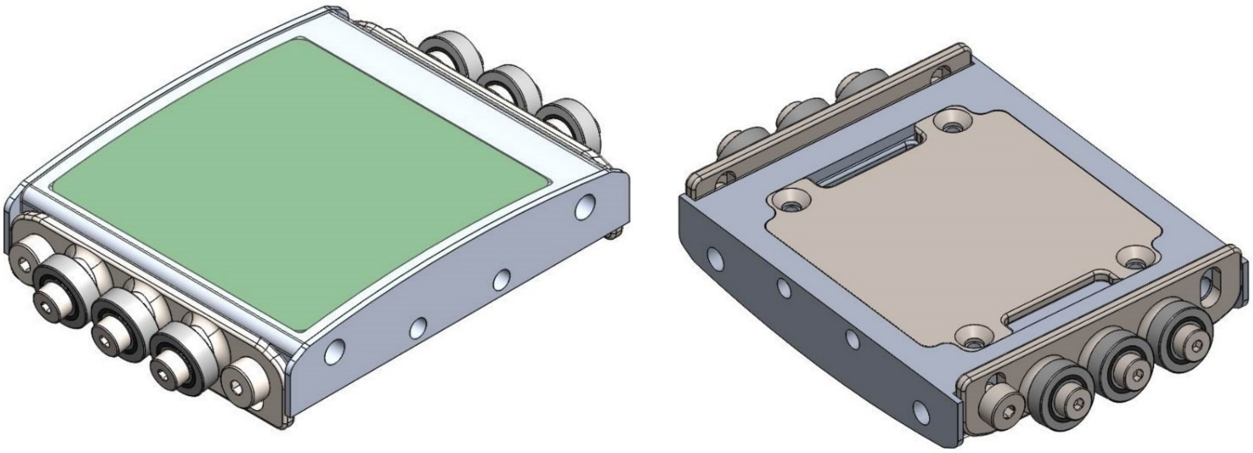

Figure 65: (L) EMAT Top Isometric View, (R) EMAT Bottom Isometric View

Figure 66 shows the prototype EMAT fabricated in ULC's shop.

Figure 66: Prototype EMAT fabricated in ULC's Shop

Design Conclusions: The conceptual design shows that incorporating guided wave EMAT with the robot and the operation of the modified robot in 24" cast iron pipe is feasible. The guided wave EMAT housings have been designed for robust and repeated use in the presence of corrosion debris and along uneven surfaces. The next steps for the guided wave EMAT integration with CIRRIS XI^{TM} would involve additional testing, and validation of liftoff sensors incorporated into the EMAT housings, further testing of the prototype EMAT housing in old pipe to validate the design, and detailed design of the robot and EMAT housings. The prototype pulser and receiver electronics will need to be updated and fabricated along with PC software. The detailed robot design will be completed including incorporating the boards and the EMATs. Following this detailed design, the fabrication and testing of the robot can be accomplished and tested in a pilot program. Additionally, there is the potential of integrating both normal beam EMAT and guided wave EMAT into the same robot. Further studies and design must be conducted to validate this.

10 PROJECT CONCLUSION

The major achievements of the project are highlighted below

1. A representative sample of pipes and defects have been studied. Numerous experiments have been performed, the results of which have proven that the EMAT guided wave is a very promising tool to inspect unpiggable pipes and small diameter pipes. Defect signatures have been identified to detect, locate and characterize the defects.
2. Wave-defect interaction has been studied by both experiment and FEA. The wave-defect interaction and its effect on the sensitivity as well as the coverage and blind zones have been studied, explained, and documented in detail.
3. A theoretical analysis tool was developed in MATLAB for dispersion analysis for both plate-like and pipe structures. The tool provides guidance for mode selection for any material-geometry combination.
4. The design of EMAT has been extensively studied by ULC. The EMAT has been optimized in various aspects including size, liftoff, and friction on pipe wall surface.
5. The automatic signal processing algorithm, i.e., damage index, has been studied and developed to aid future implementation of the technique in operation with the goal of semi-automating defect detection and assessment.
6. The selection of the baseline signal in real-world applications has also been tested. This is a promising and feasible method for inspection in the field.
7. The pipe was also tested in the soil, and it was found that the soil has minimum effect on the wave amplitude. This is because the wave propagation distance is not very long and the wave is still strong enough to be received.
8. The conceptual design has shown that the EMAT guided wave technique can be utilized on the CIRRIS XI^{TM} robot platform for inspection of unpiggable pipe. The EMATs can also be used on small diameter pipe on ILI tools.

11 FUTURE WORK

During the course of testing, a number of potential opportunities were identified for further study which falls outside of the scope of this project. The most important ones are listed here. Future studies will allow for a better understanding of guided wave EMAT design and performance for defect detection and assessment.

1. The EMAT guided wave technique has shown high potential for unpiggable pipe inspection. Moreover, the small transducer size allows for a reduction in the size and weight of current Inline Inspection (ILI) tools. Through a Department of Transportation grant, ULC will evaluate the feasibility of using EMAT guided wave to inspect multiple defects in a single ILI run while simultaneously cleaning the pipe. Such a tool will significantly increase the amount of health data collected during inspections performed every time cleaning is carried out. By employing smaller and lighter NDT sensors, the tool will be more economical to handle and operate.
2. In practical applications, many pipelines are covered by coating on the outer surface. The effect of the coating on the wave propagation and sensitivity to the defects should be studied and characterized. Also, other soil composition like clayey soil and moisture condition should be studied to represent a more realistic condition.
3. The pulsing and receiving electronics for EMAT are not commercially available for a small, unpiggable robotic system. Miniature electronics for EMAT will need to be developed to further promote the application of the technique.

4. According to API 579-1/ASME FFS-1 Fitness-for-Service, there are more defects of interest than what has been studied here. Pitting corrosion, general metal loss, and lamination can be potentially detected by guided wave also. However, making artificial defects can be tricky. If real defect samples can be obtained, additional studies can be conducted to evaluate whether EMAT guided wave can be used to inspect these types of defects.
5. The wall thinning and crack-like defects created in the shop are limited in the variety of sizes and orientations. It would be helpful to test the technique in a test facility, e.g., Pipeline Research Council International (PRCI), to fully evaluate its capability.
6. To more accurately characterize the local metal loss, the relation between defect geometry and the wave characteristics should be studied in detail by conducting more calibration work with more defect sizes. The study may also provide useful information for locating the local metal loss circumferentially.
7. To maintain the liftoff on uneven inner pipe surfaces and to minimize the cleaning requirements additional design optimization of the EMAT housing design should be performed.

GLOSSARY OF ABBREVIATIONS AND ACRONYMS

1D	1-Dimensional
3D	3-Dimensional
EMAT	Electro Magnetic Acoustic Transducer
ERW	Electric Resistance Welding
FEA	Finite Element Analysis
ID	Inner Diameter
ILI	Inline Inspection
kPa	Kilo Pascal
LRUT	Long Range Ultrasonic Testing
MHz	MegaHertz
OD	Outer Diameter
PHMSA	Pipeline and Hazardous Materials Safety Administration
PRCI	Pipeline Research Council International
Rx	Receiver
SAFE	Semi-Analytical Finite Element
SH	Shear Horizontal
SNR	Signal to Noise Ratio
STD	Standard Deviation
TOF	Time-of-flight
Tx	Transmitter
ULC	ULC Robotics